J. Space Weather Space Clim. 2025, **15**, 5

https://doi.org/10.1051/swsc/2025001

JSWSC

Available online at:
www.swsc-journal.org

RESEARCH ARTICLE OPEN ACCESS

Multi-instrument observations of ionospheric super plasma bubbles in the European longitude sector during the 23–24 April 2023 severe geomagnetic storm

Irina Zakharenkova[1,*], Iurii Cherniak[1], John J. Braun[1], Qian Wu[1,2], Sergey Sokolovskiy[1], Douglas Hunt[1], and Jan-Peter Weiss[1]

[1] COSMIC Program Office, University Corporation for Atmospheric Research, Boulder, Colorado 80301, USA
[2] HAO, University Corporation for Atmospheric Research, Boulder, Colorado, USA

Received 18 July 2024 / Accepted 16 January 2025

Abstract – This study's objective is to better specify the rare occurrence of super equatorial plasma bubbles in particular to the European longitude sector, detailing their spatio-temporal evolution, and better understanding pre-conditions for their development. Our comprehensive multi-instrument analysis combined ground-based and space observations from GNSS, ionosondes, and several satellite missions (COSMIC-2, GOLD, Swarm). We have investigated the ionospheric response to the 23–24 April 2023 severe geomagnetic storm and have shown the formation of super plasma bubbles expanding from equatorial latitudes to middle latitudes in the European/African sector during the main phase of the storm. Formation of these super bubbles was associated with storm-induced prompt penetration electric fields. We found that the area affected by the formation of numerous plasma bubbles covered more than 5000 km ranging from 30°W to 30°E in the Atlantic/African sector. The bubbles also had an impressive north-south extension, reaching as far poleward as ~30°–35° latitude in both hemispheres. After 20 UT on 23 April 2023, the zone with equatorial ionospheric irregularities reached Northern Africa, the Iberian Peninsula (Spain, Portugal) and the Mediterranean Sea in southern Europe, including areas of the Canary Islands (Spain) and the Azores and Madeira Islands (Portugal) in the Atlantic Ocean. The ionospheric irregularities persisted for 5–6 h and began to fade after ~01 UT on 24 April 2023. COSMIC-2 scintillation measurements showed intense amplitude scintillations (S4 above 0.8) across this entire region, indicating presence of small-scale ionospheric irregularities inside the extended plasma bubbles. During this storm, EGNOS (European Geostationary Navigation Overlay Service) experienced degraded performance, with significant navigation errors recorded at its southernmost stations in Northern Africa, Spain, Portugal, and their territories, which were affected by super plasma bubbles. This paper presents conclusive observational evidence showing development of the super plasma bubbles significantly expanding into the southern Europe and northern Africa region under geomagnetically disturbed conditions in April 2023.

Keywords: Super plasma bubbles / Ionospheric irregularities / Scintillations / COSMIC-2 / Geomagnetic storm

1 Introduction

Equatorial ionospheric irregularities represent a typical post-sunset quiet-time phenomenon, also known as equatorial plasma bubbles (EPB) or equatorial Spread-F (ESF). After sunset, the equatorial ionosphere becomes unstable because of Rayleigh–Taylor instability (Hysell, 2000; Kelley, 1989). Large-scale plasma density depletions can form and expand to high altitudes up to 1000 km in the vertical direction (Tsunoda et al., 1982; Woodman & La Hoz, 1976). Such plasma density depletions have east-west dimensions of ~50–250 km, can extend over 1,000 km in the magnetic north-south direction, and drift typically eastward at speeds mainly in the range of 100–200 m/s (Haerendel, 1974; Kintner et al., 2004; Mukherjee et al., 1998). Depending on season, location, and solar activity level, the quiet-time post-sunset EPBs occur primarily within a ±10°–15° range of magnetic latitudes (MLAT). The EPB phenomenon poses one of the major space weather threats to space-based communication and navigation systems in geomagnetically quiet conditions.

*Corresponding author: irinaz@ucar.edu

During geomagnetic storms, prompt penetrating electric fields (PPEFs) of magnetospheric origin can instantly impact the equatorial ionosphere and the formation of regular post-sunset EPBs. In the dusk sector, storm-induced eastward-directed electric fields amplify the regular pre-reversal enhancement electric fields, resulting in a more dramatic EPB development due to a substantial uplift of the ionosphere to higher altitudes where the Rayleigh–Taylor instability growth rate is maximized (Abdu et al., 1995, 2003; Basu et al., 2007; Huang, 2023). The storm-driven uplift of the equatorial ionosphere and plasma bite-outs can displace the storm-induced EPBs to locations far from the magnetic equator, occasionally even reaching midlatitudes, up to 35° MLAT (e.g. Basu et al., 2005). The apex altitude of these storm-induced EPBs may also be very high, exceeding thousands of kilometers above the magnetic equator (Aarons et al., 1996, 1997; Huang et al., 2007; Martinis et al., 2015). This space weather phenomenon represents one of the most challenging threats to GNSS-based operations at midlatitudes due to its unpredictability.

The term "super plasma bubble" was first introduced by Ma & Maruyama (2006) is one of the earliest reports of post-sunset plasma bubbles reaching midlatitudes (30°–34°N, 31° MLAT, Japanese sector) during the February 12, 2000, geomagnetic storm. Huang et al. (2007) described an occurrence of significant plasma density depletions linked to EPB at midlatitudes (reaching 46°–49° MLAT) in the American sector, based on the DMSP observations during the October 2003 superstorm. During the past two decades, more papers with EPB detections at midlatitudes during geomagnetic storms of different intensity have been published (Aa et al., 2018, 2019; Cherniak & Zakharenkova, 2016, 2022; Cherniak et al., 2019; Li et al., 2009; Martinis et al., 2015; Nishimura et al., 2021; Rodrigues et al., 2021; Sun et al., 2023, 2024; Zakharenkova & Cherniak, 2020, 2021) – confirming that storm-induced super plasma bubbles reaching midlatitudes is not as rare phenomenon as we thought before. Most of these papers were focused on the American and Asian longitudinal sectors.

Observational evidence of super plasma bubbles occurring in the European/African longitudinal sector is quite limited. Thus, Cherniak & Zakharenkova (2016) reported the first registration of the super plasma bubbles in southern Europe for the June 2015 geomagnetic storm using ground-based GNSS measurements [TEC (Total Electron Content) and ROTI (Rate of TEC Index change)] and in situ data of plasma density from Swarm and DMSP satellites. Ionospheric irregularities were observed for more than 8 hours in the sector ~40–45°N (~35–40°N MLAT), ~0–35°E; they were connected to the plasma bite-out in the dusk sector over west African longitudes (Cherniak et al., 2019). Katamzi-Joseph et al. (2017) reported plasma depletions in GNSS TEC and DMSP ion density observations as detected over southern Europe during the main phase of the April 2000 and 2001 geomagnetic storms. In a recent study by Campuzano et al. (2023), storm-induced ionospheric irregularities were detected over the Iberian Peninsula using data from a digital ionosonde and several GNSS stations in Spain during two moderate storms, which occurred in February 2014 and September 2021. As our observational capabilities expand, the occurrence of ionospheric irregularities at midlatitudes is becoming a subject of growing interest, particularly in Europe.

With the present study, we aim to expand the existing knowledge and database of extreme events with post-sunset super plasma bubbles in Europe by investigating their occurrence and development during the recent 22–23 April 2023 geomagnetic storm in the European/African longitudinal sector.

2 Data and methodology

We analyze the following observational data:

1) *Ground-based GNSS ROTI*: ROTI expresses the sharpness of the GPS/GNSS signal phase fluctuations caused by ionospheric irregularities and by strong spatial gradients of TEC. ROTI is calculated as a standard deviation of the time differential of TEC over 5 min (Aarons et al., 1997; Pi et al., 1997). Details of the data processing and ROTI calculation were described by Cherniak et al. (2014, 2018) and Zakharenkova et al. (2016). For this study, we utilized GNSS signals provided by the GPS, GLONASS, Galileo, and BeiDou systems. The ROTI values were computed for each GNSS satellite pass (elevation above 20°) over a ground-based station. The multisite ROTI values were binned into a geographic grid with 0.5° latitude and longitude spacing in order to generate global ROTI maps at 5-minute intervals.

2) *Multi-instrument COSMIC-2 observations*: To date, the COSMIC-2 (Constellation Observing System for Meteorology, Ionosphere, and Climate) is the largest equatorial multi-satellite constellation (six satellites) designed to study the equatorial ionosphere (Weiss et al., 2022). The scientific payloads of the COSMIC-2 mission includes an advanced GNSS receiver supporting multiple measurements including multi-GNSS TEC above and below satellite altitude, electron density profiles obtained with the radio occultation method, amplitude (S4) and phase (sigma phi) scintillations. Each satellite is also equipped with an Ion Velocity Meter (IVM) instrument (Heelis et al., 2017) to provide in situ ion density, composition, and temperature along the low inclination satellite orbits at ~525–550 km altitude, enabling simultaneous detection of EPBs across different local times/ longitudinal sectors (Zakharenkova et al., 2023). The IVM ion density was calibrated using COSMIC-2 GNSS data (Wu et al., 2022). To analyze occurrence and development of the storm-induced EPBs, we used IVM total ion density (Ni) observations, amplitude scintillation (S4) observations, and Back Propagation (BP) geolocations ("ivmLv2", "scnLv2", and "scnGeo" Level-2 products).

3) *In situ electron density* (*Ne*) observations provided by the Langmuir Probe onboard the Swarm B polar-orbiting satellite operated at ~500 km altitude. The Swarm electron density data is accessible as a Level-1b product ("EFIxLPI_1B") on the European Space Agency Earth Online portal. The Swarm mission consist of the three satellites – A, B, and C. Here, we used only Swarm B measurements, as its orbit was located in the evening sector during the April 2023 storm. The Swarm B crossed the equator around 7.9 LT and 19.8 LT.

4) *Global-Scale Observations of the Limb and Disk* (*GOLD*) night-time optical images of atomic oxygen 135.6-nm emissions.

5) *Ionosonde ionograms* recorded by the El Arenosillo digisonde station in Spain.

6) *Scintillation measurements* provided by INGV (Istituto Nazionale di Geofisica e Vulcanologia) scintillation receiver in Lampedusa, Italy.

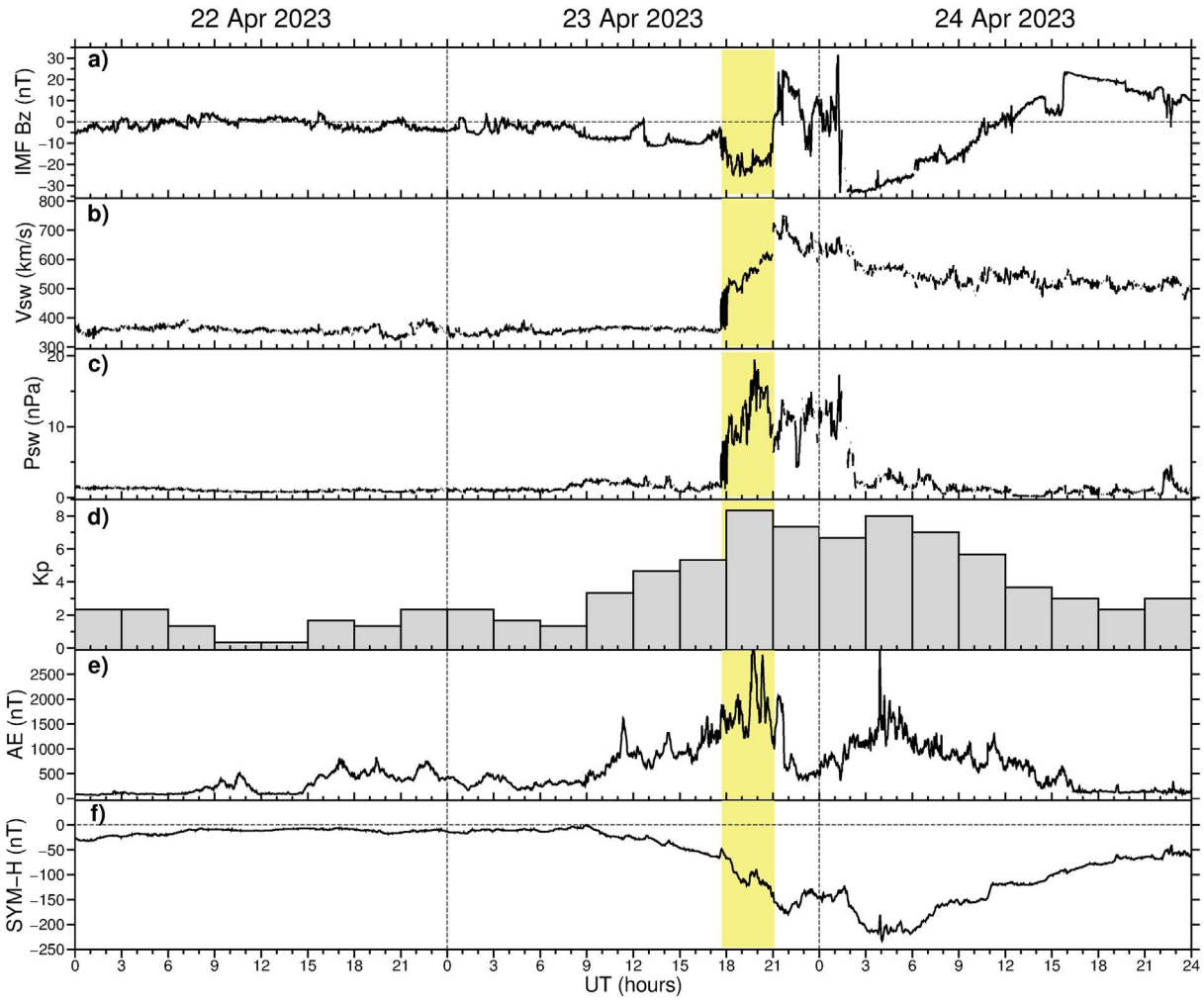

Figure 1. (a) Interplanetary magnetic field (IMF) Bz component, (b) velocity, and (c) dynamic pressure of the solar wind, (d) 3-h *Kp* index, (e) SuperMAG auroral electrojet index AE, and (f) SYM-H index during 22–23 April 2023. The yellow shading shows time when plasma bite-outs and strong equatorial plasma bubbles formed in the European/African sector.

7) *EGNOS* (*European Geostationary Navigation Overlay Service*) positioning accuracy performance reports.

3 The April 2023 Geomagnetic storm: space weather conditions

The coronal mass ejection (CME) which erupted from the Sun on 21 April 2023 resulted in a severe geomagnetic storm on the Earth on 23–24 April 2023. The shock hit the Earth's magnetosphere at ~17:45 UT on 23 April 2023. Figure 1 presents variations of the solar wind, interplanetary, and geophysical parameters during 22–24 April 2023. The geomagnetic storm commencement was registered at 17:45 UT on 23 April 2023 with a rapid increase of solar wind velocity, going from ~350 km/s to 500 km/s (Fig. 1b), and of solar wind pressure from ~2 to 8 nPa (Fig. 1c). The interplanetary magnetic field (IMF) north-south component Bz was near −5 nT just before the storm started at ~17:45 UT (Fig. 1a). After that, it turned southward down to −20 nT and remained steady southward (−20 to 25 nT) for several hours until ~21 UT on 23 April 2023, thus maintaining the magnetic field reconnection at the Earth's magnetopause. At 21 UT, the IMF Bz turned northward. In Figure 1f, the SYM-H provides the strength of the equatorial ring current and, consequently, the geomagnetic storm. During the first main phase of the storm that lasted until ~22 UT, the SYM-H reached a minimum of −179 nT with another intermediate minimum of −121 nT at 19:25 UT. Later, during the second main phase of the storm, which lasted from ~01 until 04 UT on 24 April 2023, the SYM-H reached a minimum of −218 nT. The AE (auroral electrojet) index increased above 500 nT after ~09 UT on 25 August 2018, and multiple AE peaks exceeding 1,000–1,500 nT were registered during 18–22 UT on 23 April 2023 (Fig. 1e). During 18–21 UT on 23 April 2023, the 3-h Kp index reached value of 8+ (Fig. 1d), corresponding to a G4 "severe" level in NOAA's geomagnetic storm classification.

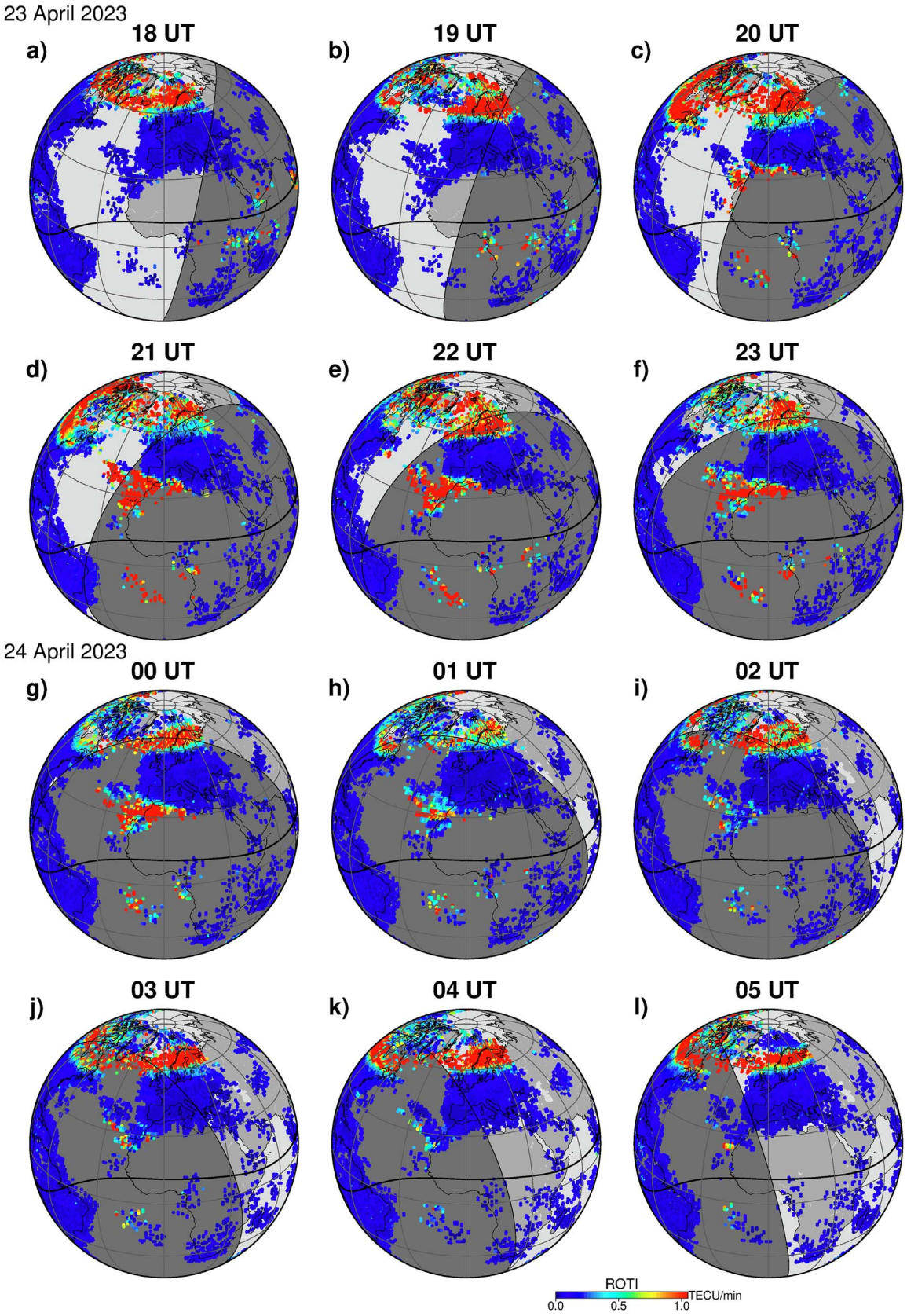

Figure 2. Ground-based GNSS ROTI observations during 18–05 UT on 23–24 April 2023. The grey shading shows nighttime, and the thick black line is the magnetic equator. The central meridian is 0° and the longitude/latitude grid has a 30° interval. High ROTI values (intense red color) depict strong ionospheric irregularities of equatorial and auroral origin.

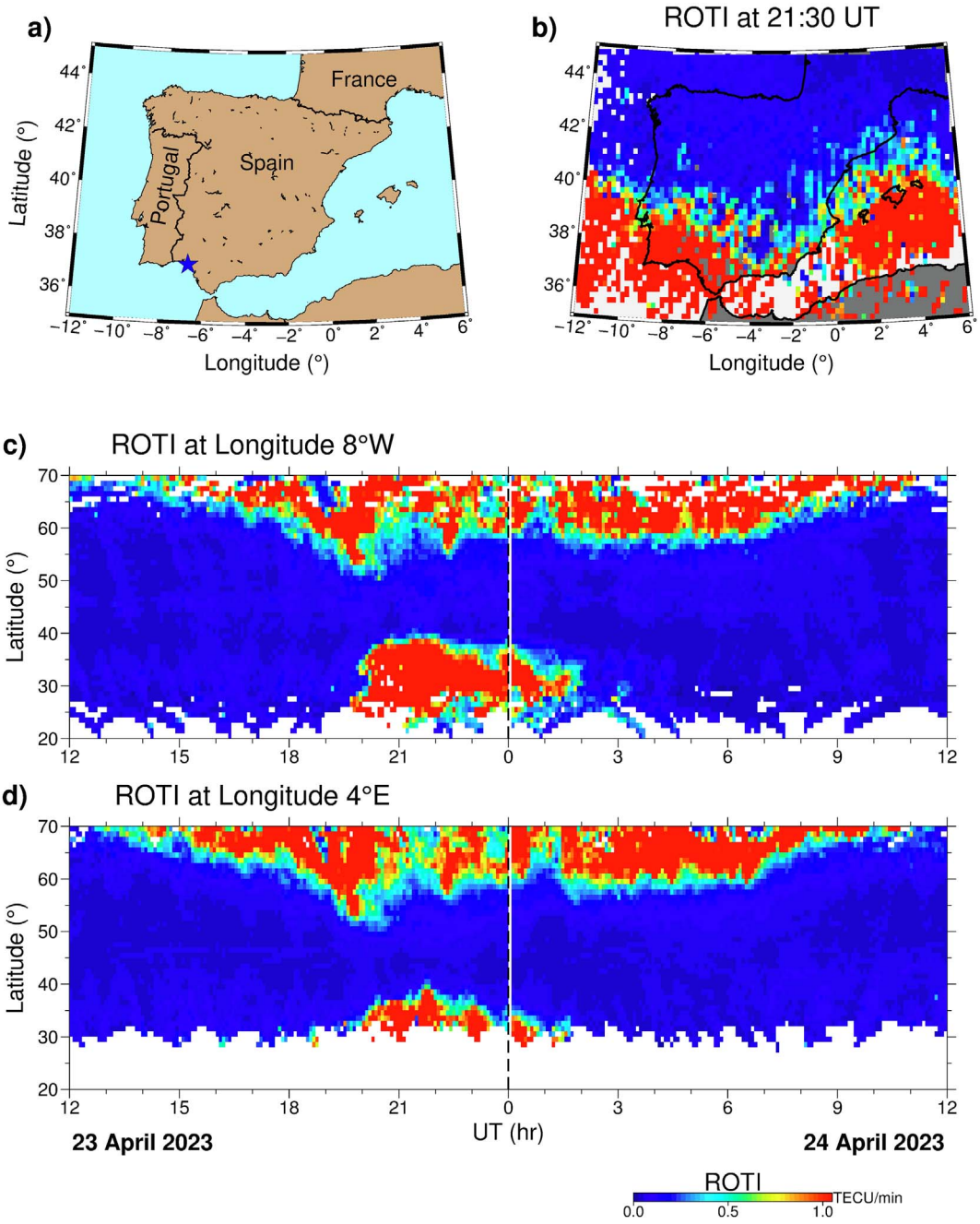

Figure 3. (a) Map of south-western Europe with Spain and Portugal borders. (b) High-resolution ground-based GNSS ROTI observations over this region for 21:30 UT on 23 April 2023. (c–d) GNSS ROTI keograms representing spatio-temporal signatures of storm-induced plasma disturbances at two different longitudes (4°E and 8°E) in south-western Europe on 23–24 April 2023. White/blank cells at the bottom are due to the data absence. The location of the El Arenosillo digisonde station in southern Spain is shown as a blue asterisk on map (a).

4 Results

4.1 Ground-based GNSS observations

We present an overview of the storm-induced ionospheric plasma density irregularities of equatorial origin that reached European midlatitudes in the main phase of the April 2023 geomagnetic storm. We examined the ground-based GNSS data and used the GNSS ROTI mapping technique to identify and geolocate ionospheric irregularities in regions with dense networks of ground-based GNSS stations.

Figure 2 presents a sequence of the GNSS ROTI maps centering on the European/African sectors (0°E central meridian) for selected epochs on 23–24 April 2023 during the main phase of the storm. We have excellent data coverage in the European region (30°–80°N latitude) due to very dense regional

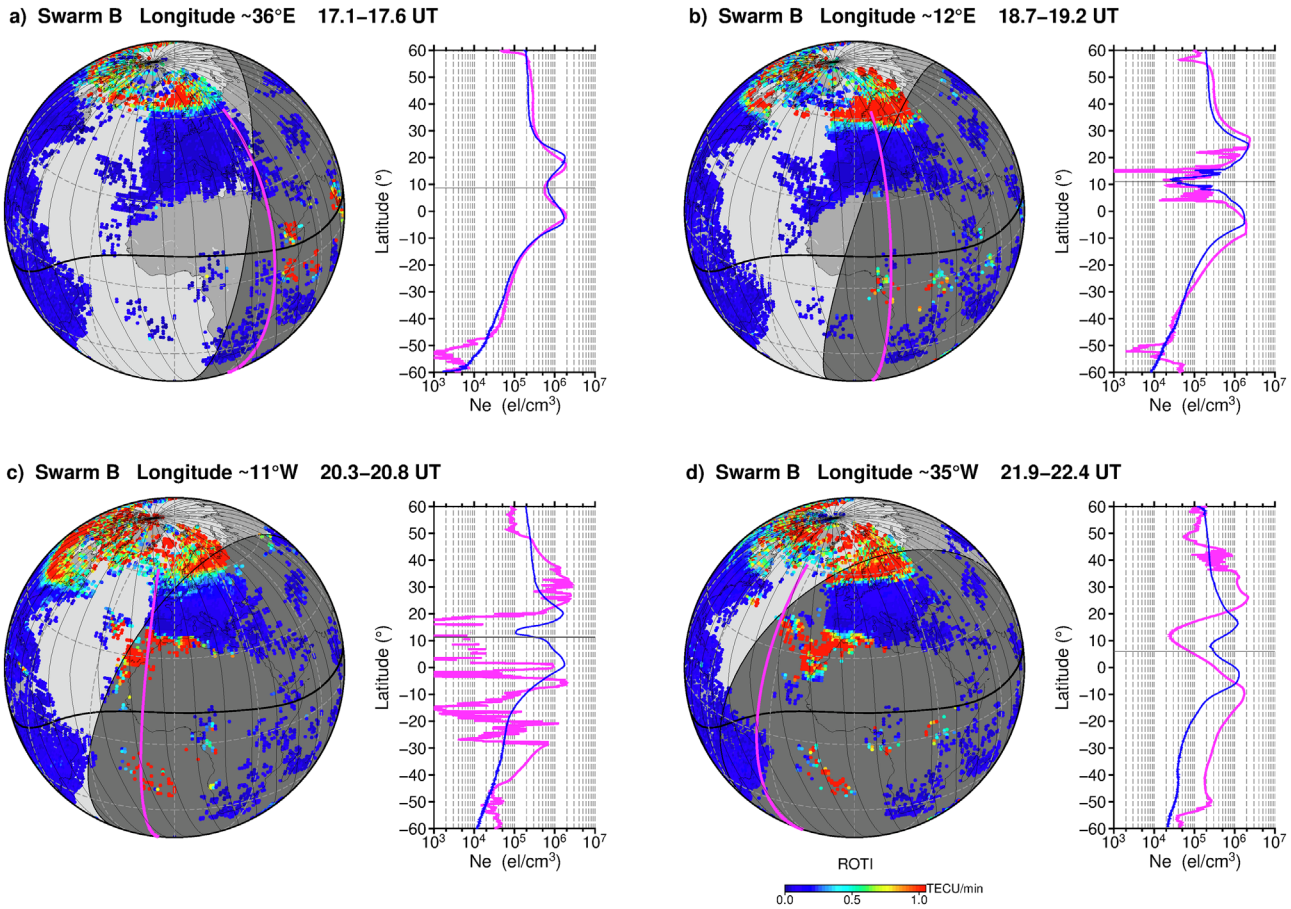

Figure 4. (a)–(d) Sequence of several consecutive Swarm B satellite overpasses (magenta line) plotted over GNSS ROTI maps during 17–22 UT on 23 April 2023, along with Swarm in situ electron density (Ne) variations plotted as a function of geographical latitude for the storm day (magenta line) of 23 April 2023 and the reference day (blue line) of 22 April 2023. The thin horizontal line on density plots marks the magnetic equator location.

and national networks of GNSS stations. However, there is a significant data gap in central Africa due to the lack of ground-based stations.

The first ROTI map on Figure 2a shows conditions at 18 UT on 23 April 2023, at the beginning of the storm. Here we already see increased auroral activity (AE index was larger than 1,000–1,500 nT; Fig. 1e) depicted as an expanded zone of the auroral irregularities oval at high latitudes of the Northern Hemisphere. The intense auroral ionospheric irregularities (ROTI > 0.8–1 TECU/min) were detected well down to 60°N. Also, there are some signatures of the post-sunset EPBs in the eastern African and Indian sectors (eastward of 30°E). Over the next hour (Fig. 2b), signatures of intense ionospheric irregularities associated with post-sunset EPBs progressed further westward, to the west coast of central Africa (~10°E).

Starting from 20 UT on 23 April 2023 (Fig. 2c), the ROTI maps reveal equatorial irregularities extending to Northern Africa, covering a range of 15°W – 15°E in longitude and 25°–35°N in latitude. Since we have proper data coverage across Europe, we can confirm the absence of ionospheric irregularities in the central part of Europe, shown by a wide band of blue color, that acts as a dividing boundary between the southern zone with ionospheric irregularities from Africa and the northern zone with the high latitude auroral irregularities. The existence of several GNSS stations on islands in the Atlantic Ocean enabled us to detect ionospheric irregularities in the conjugate region in the Southern Hemisphere too. Notably, ionospheric irregularities in central and southern Africa occurred in the post-sunset, but those expanding to Northern Africa stretched into the sunlit ionosphere ahead the sunset terminator passage.

In the next few hours between 21 and 00 UT (Figs. 2d–2g), the zone with equatorial ionospheric irregularities, already reaching Northern Africa and the Iberian Peninsula in southern Europe, continued to expand further north-westward, including to areas of the Canary Islands (Spain) and the Azores and Madeira Islands (Portugal) in the Atlantic Ocean. This zone, spanning 20°–40°N latitude and 35°W–15°E longitude, extended over 5000 km (~50° longitude). The intense ionospheric irregularities remained present for 5–6 h in this area and began to fade after ~01 UT on 24 April 2023 (Figs. 2h–2l).

The ground-based GNSS ROTI data showed very intense ionospheric irregularities stretching far north and south from the magnetic equator covering large parts of Northern Africa and southwestern Europe. In the southern European mainland, this mainly corresponds to the Iberian Peninsula region, which

encompasses Spain and Portugal. To provide a closer look at this region, Figure 3a presents a map of the Iberian Peninsula, featuring the borders of Spain and Portugal. Figure 3b shows a snapshot of high-resolution ROTI maps for that region at 21:30 UT on 23 April 2023. We can see that the ionospheric irregularities reached as far north as ~40°N, impacting the southern parts of Portugal and Spain. Also, intense ionospheric irregularities were detected in the western Mediterranean Sea, here on this map over 6°W–6°E, in particular affecting regions of the Spanish Balearic Islands Mallorca and Menorca.

To better illustrate the evolution of storm-induced ionospheric irregularities in southern Europe, we examined two particular longitudes: 8°W (approximately the border between Spain and Portugal) and 4°E (near the Mallorca and Menorca islands). Figures 3c–3d display keograms of ROTI for 23–24 April 2023 along longitudes 8°W and 4°E. The keograms show the average ROTI value within a ±1.5° band around a selected longitude, plotted against time (UT) and geographic latitude. For higher latitudes (poleward of ~60°N), the ROTI keograms show a similar pattern – intense ionospheric irregularities occurred in this sector after ~14 UT on 23 April 2023. The zone with auroral irregularities expanded from high latitudes toward midlatitudes and reached as far south as 54°N during 19–20 UT, when the AE index had peak intensification above ~2,000 nT (Fig. 1e). Also, very intense high latitude irregularities were observed over 60–70°N during 22–08 UT into the next day of 24 April 2023. Most of the European midlatitudes were in a zone with an absence of ionospheric irregularities (blue color on Figs. 3c–3d). After ~20 UT, an area with intense ionospheric irregularities rapidly emerged from the south, extending as far north as 40°N. The northward expansion of ionospheric irregularities appears to be stronger in the western longitude (8°W; Fig. 3c) than in the eastern longitude (4°E) in the Mediterranean region. That can be explained by the north-westward tilt of ionospheric irregularities seen in Figures 2c–2f, as irregularities were stretched largely towards the central part of the Atlantic Ocean. The ionospheric irregularities affected the region from ~20 UT on 23 April to ~02 UT on 24 April 2023. Throughout that period, the ionospheric irregularities originating from the south were well isolated from the zone of high latitude auroral irregularities that affected Europe from the north.

4.2 Swarm in-situ observations

The large data gaps in ground-based GNSS observations in central Africa make it difficult to trace the evolution of storm-induced EPBs over the region of its direct origin if relying solely on this data source. Fortunately, satellite observations allow us to partially reconstruct the picture. Here, we analyzed in situ plasma density data from the Swarm B satellite in a polar orbit of ~88° inclination with an orbit altitude of ~500 km. On 23 April 2023, Swarm B crossed the equator around 19.8 LT, which was a very fortunate local time just after sunset, allowing us to trace the initial phase of the EPB development.

Figure 4 shows a series of four consecutive Swarm B overpasses that occurred in the African longitudinal sector at the proper time, from 17 to 22 UT on 23 April 2023. Figure 4a depicts the situation for 17.1–17.6 UT on 23 April 2023, prior to the storm onset. The Swarm B satellite passed over the eastern African region near 36°E. The satellite trajectory was slightly westward from the area where the ionospheric irregularities were detected in ground-based ROTI data over the eastern African and Indian sectors. The Swarm B in situ density observations showed no irregularities over the equatorial and low latitude regions; density variation was very smooth with the two crests of the equatorial ionization anomaly (EIA), whose locations and magnitude were quite similar to the conditions on the previous quiet day (blue line on Fig. 4a, right). The next Swarm overpass was near 12°E in central Africa during 18.7–19.2 UT (Fig. 4b). It encountered a wide depleted region near the equator and plasma density structures over 0°–22°N (~ ±10° MLAT), which may correspond to the beginning stage of the storm-induced EPBs development over central Africa. Figure 5c presents the situation after 20 UT. The ground-based ROTI observations showed an expansion of the intense ionospheric irregularities from the equatorial region towards much higher latitudes, as far as ~10°–25°S to the south and ~25°–35°N to the north towards northern Africa and southern Europe. The Swarm B satellite next went over the western Africa region near 11°W. At an altitude of ~500 km, the Swarm B encountered a wide plasma bite-out over the magnetic equator as broad as 20° in latitude and strong plasma density structuring and depletions at ~25–35°N and 0–30°S. The large extension of these ionospheric structures from equatorial to higher latitudes covered the range of EPB apex height from ~1500 km to ~3000 km. The Swarm in situ plasma density observations during the storm differ drastically from the density variation in the previous quiet day (blue line, Fig. 4c, right). The next Swarm B pass over the region was near 22 UT at ~35°W longitude in the Atlantic Ocean (Fig. 4d). The satellite in situ plasma density measurements showed a largely intensified EIA with a very deep and wide trough near the equator, the crests were displaced to ~26°N and ~11°S, corresponding to ~18° MLAT. Unlike in two previous overpasses, there were no irregular structures or depletions observed between the EIA crests at equatorial latitudes. However, a small area with plasma density structuring was detected between latitudes 36°–44°N, further poleward from the northern crest of the EIA. This detection aligns with the high ROTI values observed in this region (Fig. 4d), corresponding with the area of intense ionospheric irregularities extending from northern Africa towards the Atlantic Ocean in the northwest direction.

Thus, Swarm in situ observations confirmed the presence of strong ionospheric irregularities over the African sector during the storm's main phase. It also shows clear evidence that intense ionospheric irregularities along the magnetic equator were confined to a limited longitude range, for just two orbits (Figs. 4b and 4c).

4.3 COSMIC-2 in-situ observations

The ability to detect EPB signatures in satellite in situ plasma density observations greatly depends on the satellite orbit inclination. For polar orbiting LEO (Low-Earth-Orbit) satellites, each successive orbit will cross the equator approximately 20°–25° further west in longitude than the previous one (e.g. Swarm B passes on Fig. 4), meaning no re-visiting of the same geographical area for at least the next 10–12 h. This restricts the ability of a single polar orbiting satellite to trace how EPBs evolved in a particular longitudinal sector. Satellites in low inclination orbits are the only ones able to revisit equatorial and low latitude regions multiple times daily, increasing the chances of encountering the same plasma depletion

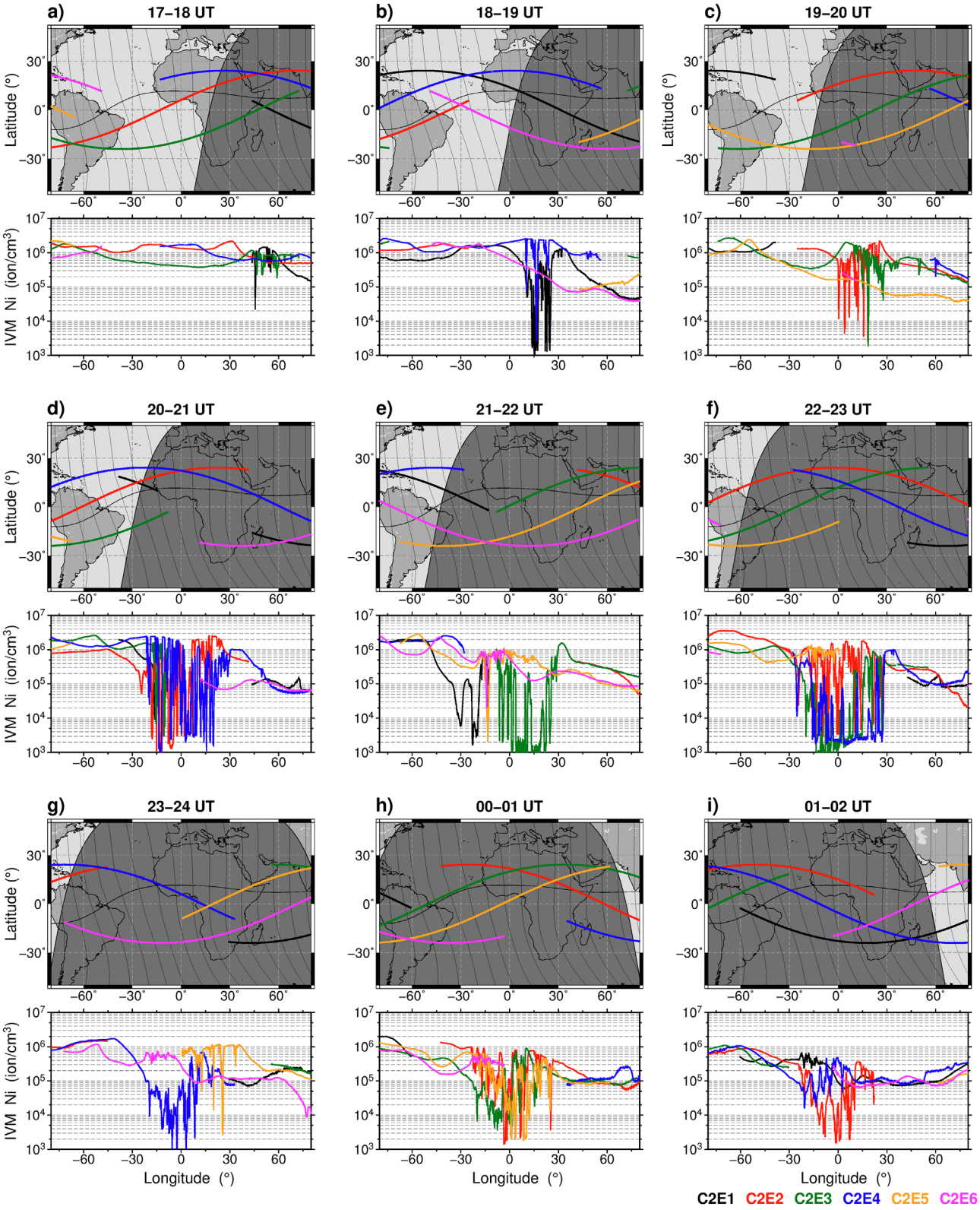

Figure 5. COSMIC-2 satellite tracks (color-coded) and IVM in situ ion density (Ni) along these tracks for a sequence of 1-h time intervals (a)–(i) during 17–02 UT on 23–24 April 2023. The thin black line on the maps marks the magnetic equator, the grey shading shows nighttime.

structure again – for example, the Communication/Navigation Outage Forecasting System (C/NOFS) satellite (Huang et al., 2011, 2013).

Launched in 2019, the COSMIC-2 equatorial constellation represents the largest satellite-based observational system designed to study the equatorial ionosphere (Weiss et al., 2022). For the COSMIC-2 mission, the configuration of six satellites distributed evenly around the globe in a ~24° inclination orbit provides an opportunity to encounter plasma depletion structures with a sampling rate that is much faster than any single satellite could provide. Figure 5 gives an overview of storm-induced plasma depletions development in the European/African longitudinal sector as detected by COSMIC-2 IVM in situ density measurements. With six satellites in low-inclination orbits, we can achieve multiple satellite encounters in the sector of interest within 1 h – that can support detection of plasma depletions by multiple satellites and offer insights into the latitudinal variations of those depletions. Six COSMIC-2 satellites are marked as C2E1 to C2E6.

The first map for 17–18 UT on 23 April 2023 (Fig. 5a) demonstrates that several COSMIC-2 satellite tracks took place over Africa, with predominantly smooth ion density variations along these tracks. Moving further east from Africa, the two satellites C2E1 and C2E3 (black and green lines, respectively) encountered plasma density depletions in the area between 45°–60°E. The next map in Figure 5b illustrates the conditions for 18–19 UT just after the onset of the geomagnetic storm, coinciding with sunset over central Africa. Here C2E1 and C2E4 observed deep plasma density depletions (rapid drops in plasma density by several orders of magnitude) in the area spanning 10°–25°E in longitude. C2E1, positioned closer to the magnetic equator, detected significantly stronger depletions compared to C2E4 overflying Northern Africa at ~25°N (~15°N MLAT). Another satellite C2E6 (magenta line on Fig. 5b) crossed southern Africa at ~30°–35°S MLAT and did not observe any irregularities in plasma density variations. In the following hour, 19–20 UT (Fig. 5c), C2E2 (red line) crossed the magnetic equator in Africa. Observations show that the region with intense plasma density depletions extends further west (following the sunset terminator), now covering a longitudinal range of 0°–25°E.

Figure 5d shows the situation for 20–21 UT, when the entire African longitudinal sector was in post-sunset conditions. The storm has already been developing for several hours, with a steady southward IMF Bz (Fig. 1). Here C2E2 and C2E4 appeared in Northern Africa and recorded a drastic evolution of the ionospheric irregularity area—plasma bubbles became much more frequent (trains of bubbles) and very intense (drops by 2–3 order of magnitude relative to the background density) and they now covered a broad area of more than 50° in longitude, ranging from 25°W to 25°E. The next map shows the development of the situation for 21–22 UT (Fig. 5e). At that time, only one satellite, C2E3 (green line), passed through the equatorial region of central Africa. It detected broad plasma density depletions and signatures of plasma bite-outs between 10°W and 30°E (Fig. 5e, bottom plot), that started not from 10°W but rather from 18°W in the previous hour (Fig. 5d, green line in bottom plot). When two other satellites C2E5 and C2E6 passed over the same region in the Atlantic Ocean near ~15°W in longitude and ~26°S (~35°S MLAT) in latitude, they both observed a deep plasma density depletion over this region, meaning that plasma bubbles had already extended to ~35° MLAT in the Southern Hemisphere. This is consistent with ground-based ROTI observations that detected intense irregularities over that part of the Atlantic Ocean during 21–22 UT (Figs. 2d and 2e). With low inclination satellites, our observational range is restricted by orbits, making it difficult to assess the full latitudinal (north–south) extent of the EPB structures. Nevertheless, for the depletion identified by two satellites at (26°S, 15°W), the estimated apex altitude was very high, ~3000 km. C2E1 crossed the magnetic equator near 35°W and detected here a broad depletion in plasma density that was different from the typical signature of plasma bubbles. This depletion is most likely related to a strong deepening of the trough during intensification of the EIA, as observed by the Swarm B satellite directly over that area (Fig. 4d). During 22–23 UT (Fig. 5f), three satellites, C2E2, C2E3 and C2E4, passed over central and northern Africa. They all detected further evolution of the zone affected by intense plasma density depletions, now extending nearly 6000 km in longitude, from 30°W to 30°E. The satellite tracks of C2E3 and C2E4 were closer to the magnetic equator, and they encountered significant plasma density depletions (drops in plasma density of ~3 orders of magnitude). During the next few hours (Figs. 5g–5i), COSMIC-2 satellites passing over the African sector observed numerous plasma density depletions, which persisted into the later post-midnight time.

It is important to emphasize that in situ observations from different COSMIC-2 satellites clearly showed that the storm-induced ionospheric irregularities in the African longitudinal sector were confined to the same longitudinal range between 30°W and 30°E from ~20 UT on 23 April (~1–2 h after sunset) to later into the night. That can explain the absence of the equatorial irregularities detected during the Swarm B crossing near 35°W longitude after 22 UT on 23 April 2023 (Fig. 4d) – that orbit location was just outside the longitude range where the strong plasma depletions formed.

From this, we see the effectiveness of COSMIC-2 in situ measurements from multiple satellites in tracing the occurrence and evolution of the equatorial ionospheric irregularities during geomagnetic disturbances. We also see the advantages and limitations of different satellite orbit inclinations, comparing polar and equatorial orbits. We can definitely obtain more valuable information from the combination of satellite observations at various orbits, if the data are available.

Figure 6 presents an example of combining data from different missions, Swarm and COSMIC-2, both orbiting at ~500–550 km altitude. The satellites traversed through the European/African longitudinal sector at 20–21 UT on 23 April 2023. This Figure provides a more in-depth view of what we previously discussed in Figures 4 and 5. The polar-orbiting satellite Swarm B crossed the sector from 50°N to 30°S, moving southward along ~11°W longitude, during 20.32–20.67 UT. From an altitude of ~500 km, it detected signatures of midlatitude irregularities at ~25–37°N in north-western Africa and just westward from the Iberian Peninsula and Gibraltar, and a broad area of plasma bite-out near the magnetic equator between latitudes 20°N and 0°N.

At around the same time, from 20.30 UT to 20.62 UT, the COSMIC-2 satellite C2E4 passed over the region of Northern

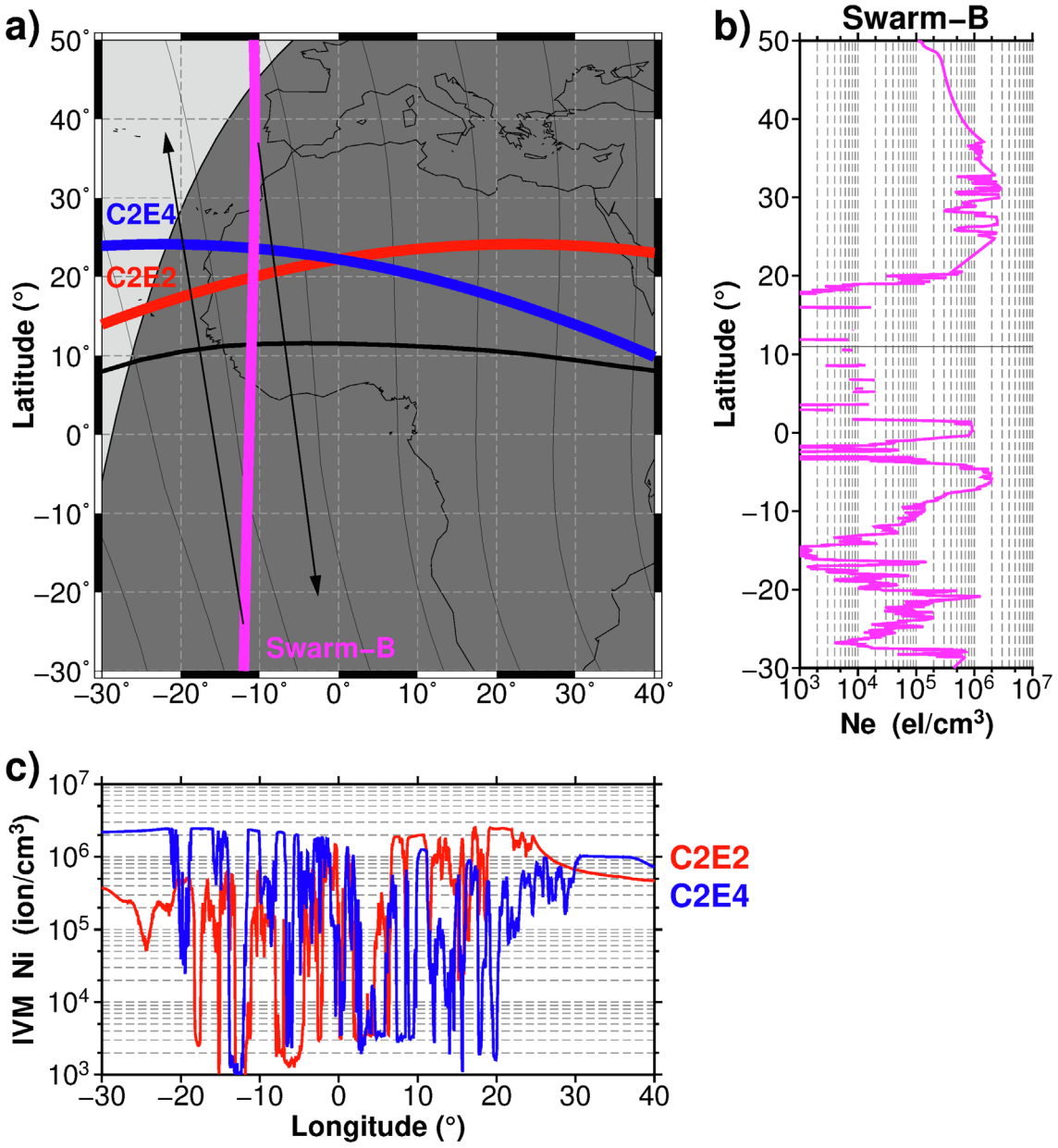

Figure 6. Combined view of in situ ion/electron plasma density in the European/African longitudinal sector at 20–21 UT on 23 April 2023. (a) Geographical location of satellite overpasses: Swarm B and two COSMIC-2 C2E2 and C2E4. The thick black line marks the magnetic equator, the thin gray lines are magnetic field lines, the shaded area shows nighttime. The arrows point towards the conjugate points from the midlatitude irregularities detected by Swarm B. (b) Corresponding in situ electron density (Ne) variations along the Swarm B pass (20.32–20.67 UT) plotted as a function of geographical latitude. (c) Corresponding in situ ion density (Ni) variations along COSMIC-2 C2E2 and C2E4 passes (20.68–20.98 UT and 20.30–20.62 UT, respectively) plotted as a function of geographical longitude.

Africa from west to east. Roughly 23 min later, C2E2 crossed the Northern Africa region on a trajectory that was relatively close to C2E4. The orbit altitudes were ~525 km and 530 km for C2E4 and C2E2, respectively. Both COSMIC-2 satellites observed numerous intense plasma density depletions spanning between 20°W and 20°E in longitude. Near the longitude of 11°–12°W, where the Swarm B detected a plasma bite-out over the equatorial latitudes, both COSMIC-2 satellites showed the presence of a plasma density depletion of approximately 4–5° wide in the west–east direction with a density drop of ~2.5–3 orders of magnitude. Due to the westward tilt of plasma bubbles in this region (see the magnetic field line directions on the map), the depletion located slightly further west for C2E4, whose track was more northward than the C2E2 track. This perspective reveals that the Swarm B trajectory passed directly through this depletion zone of ~4–5° wide. Thus, COSMIC-2 satellites, intersecting this depletion in the zonal direction, measured a width of ~4–5° in longitude, while

concurrent Swarm B intersection in the meridional direction revealed that this depletion had a latitudinal elongation of ~20° (within ±10° MLAT around the magnetic equator). It is important to emphasize that this was just one of many structures detected by COSMIC-2 between 20°W and 20°E (Fig. 6c), which Swarm B satellite could not observe. In addition, if we follow the direction of magnetic field lines (as shown by the southward arrow in Fig. 6a), then the irregularity structures seen by Swarm B at midlatitudes around 25°–37°N and along ~10–11°W are most likely linked to another wide plasma density depletion detected by the C2E2 satellite between 8°W and 4°W in longitude. The intense irregular structures that Swarm B encountered in the Southern Hemisphere near 10°–28°S had their conjugate projections near 30°–38°N in the sunlit region of the Northern Hemisphere (as shown by the northward arrow in Fig. 6a). Hence, the equatorial ionospheric irregularities that were formed over western Africa in the post-sunset period, rapidly extended further poleward, partially appearing in the pre-sunset region of the Atlantic Ocean. Their occurrence in these distant latitudinal regions at ~20–30°S and ~25–35°N were well confirmed by ground-based ROTI observations (Figs. 4c and 2c–2f).

4.4 COSMIC-2 amplitude scintillation observations

The Swarm and COSMIC-2 satellites measured ionospheric in situ plasma density at ~500–550 km altitude, revealing the formation of intense ionospheric irregularities after the storm onset in the African sector spanning between 30°W and 30°E in longitude and extending as far poleward from the magnetic equator as ~30°–35° latitude in both hemispheres. The important question is how active these plasma bubbles are in terms of producing amplitude scintillations in the radio signals that travel through the medium. Here, we propose to examine another type of ionospheric observations provided by the COSMIC-2 mission, specifically scintillation observations. The commonly used scintillation indices for measuring the amplitude and phase scintillations are S4 and σ_{φ} (sigma_phi), respectively (Basu et al., 1985; Fremouw et al., 1978). The S4 index is the standard deviation of the received power normalized by its mean value, and the phase scintillation index is the standard deviation of the detrended carrier-phase measurements. In this paper, we used the Level-2 product "scnLv2" with amplitude (S4) and phase (sigma_phi, σ_{φ}) scintillation indices, which are computed on the ground from the high-rate observations from the Tri-GNSS (Global Navigation Satellite System) Radio-occultation System (TGRS) instrument onboard the COSMIC-2 (e.g. Weiss et al., 2022). TGRS calculates an on-board S4 index at a 10-second cadence for every GNSS satellite it tracks via its precise orbit determination antennas. The time history of the S4 index is evaluated for every ionospheric occultation observed by TGRS. If the on-board S4 index exceeds a programmable threshold of 0.1 at any point within an occultation, TGRS triggers mechanism to transmit high-rate (100 Hz for GLONASS and 50 Hz for GPS) phase and amplitude data to the ground. The COSMIC Data Analysis and Archive Center (CDAAC) provides these high-rate scintillation data as COSMIC-2 Level-1 "scnPhs" product. High-rate phase and amplitude data collected by the TGRS are also processed into S4 and sigma_phi scintillation indices products. These two scintillation indices are computed using a sliding window of 10 s of data but are output at 1-second intervals. The results are provided as "scnLv2" product and only available when the on-board S4 index exceeds this specific threshold.

In "scnLv2" files, these scintillation indices are provided with a 1-Hz rate for L1 and L2 frequencies for both GPS and GLONASS systems, along with Earth-Centered-Earth-Fixed coordinates for COSMIC-2 satellite position and GNSS satellite position. If we detect the existence of ionospheric irregularities or scintillations on the line-of-sight link between a GNSS receiver and a GNSS transmitter, the exact location of these irregularities and their spatial extent along this link remain unknown. One possible approach is to assign the location of detected ionospheric irregularities to the location of the LEO satellite at that time, while another simplest and commonly used approach is to assign it to the tangent point, which is the closest point along the LEO–GNSS line to the Earth's surface (e.g. Dymond, 2012; Ko & Yeh, 2010). Generally, each ionospheric occultation extends over a range of tangent point altitudes from ~90 km up to the COSMIC-2 satellite altitude. In this paper, we also assigned the S4 amplitude scintillation values to the tangent point location, and then, for each file within the range of altitudes of this particular ionospheric occultation, we determined the highest S4 value (S4max) that should have a tangent point altitude above 120 km (to exclude scintillations related to the sporadic E layer). We utilized the amplitude scintillation data for L1 frequency only.

Figure 7 presents an overview of COSMIC-2 amplitude scintillation detections in terms of space-observed S4max during 14–06 UT on 23–24 April 2023. For each occultation file, the single maximal S4 value exceeding 0.2 is plotted at its tangent point location, while the intensity of S4 is depicted by the size of the blue circles centered around the respected tangent point. Before the dusk sector moved into the African region (Figs. 7a–7b), amplitude scintillations were observed over the Indian Ocean at equatorial latitudes. During next 2 h after the storm commencement at 17:45 UT (Fig. 7c), strong amplitude scintillations with S4 > 1.0 were detected over equatorial and low latitudes of central Africa at ~15°–30°E, as well as several detections over western Africa at 5°W–5°E stretching to higher latitudes towards Northern Africa and Europe. During 20–22 UT (Fig. 7d), amplitude scintillations with S4 exceeding 0.5–1.0 were often detected over equatorial and low latitudes of central Africa, covering a broad longitude range of ~0°–30°E. Moving further westward into the Atlantic Ocean to ~30°W longitude, multiple detections with elevated S4 were observed in both hemispheres stretching between ~35°N and ~30°S. These localizations match very well with areas of high ROTI detections in ground-based GNSS data during 20–22 UT (Figs. 2c–2e). Over the next 4 h (Figs. 7e–7f), numerous cases with increased amplitude scintillations (S4 > 0.8–1.0) were detected over the African longitudinal sector between 30°W and 30°E and with a latitudinal extent as far poleward as 30°N and 30°S. After 02 UT on 24 April 2023 (Figs. 7g–7h), the intensity of the amplitude scintillations detected in this region started to weaken as sunrise approached.

From this we see that the COSMIC-2 space-based observations provides observational evidence that strong amplitude scintillations occur precisely over regions with extended ionospheric irregularities which were detected by ground-based GNSS and LEO satellite in situ observations.

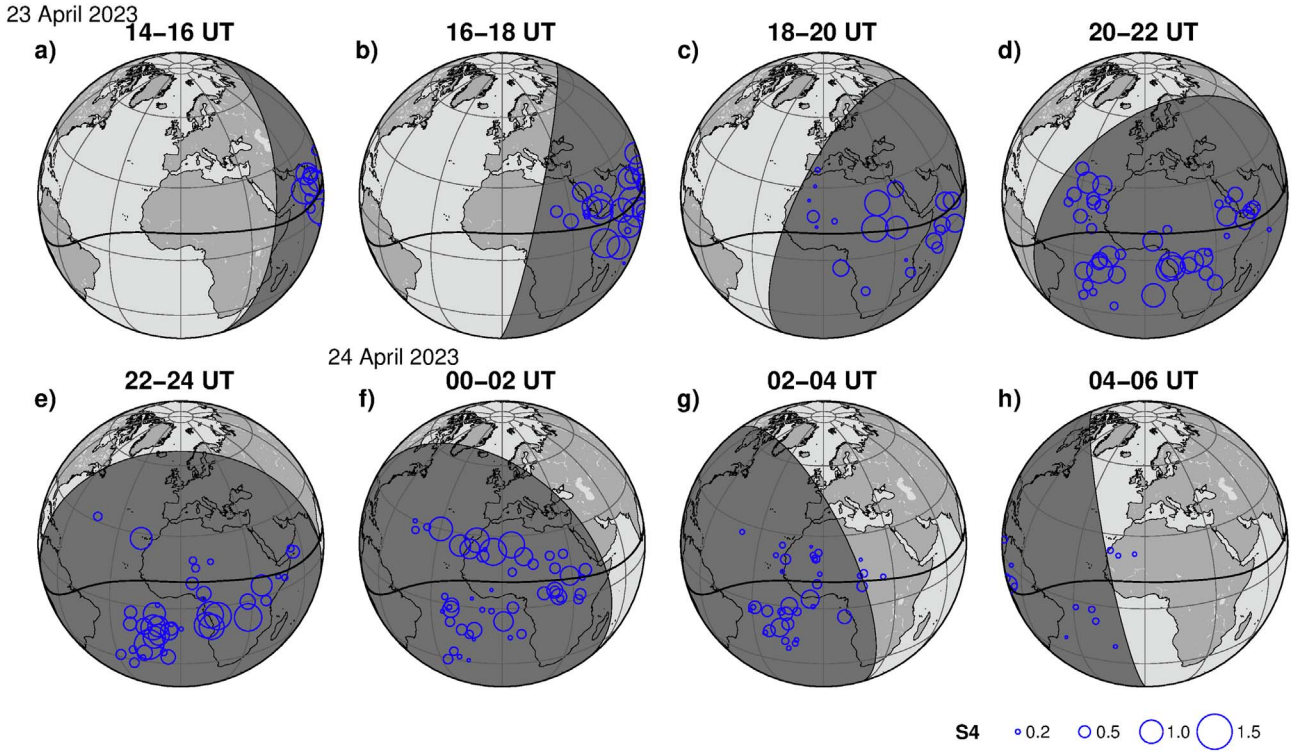

Figure 7. (a)–(h) COSMIC-2 amplitude scintillation S4 detections for specific 2-h time intervals during 14–06 UT on 23–24 April 2023. The circle size is proportional to the S4 magnitude. The central meridian is 0°, the grid has a 30° increment in latitude/longitude. The grey shading shows nighttime, the thick black line is the magnetic equator.

4.5 COSMIC-2 back propagation geolocations

As mentioned earlier, the precise localization of ionospheric irregularities remains a key challenge in the application of remote sensing RO techniques for monitoring ionospheric irregularities. To achieve more accurate localization of the ionospheric irregularities along the ray path from GNSS transmitter to LEO receiver, more advanced and sophisticated approaches can be utilized, such as the multiple phase screen method with the forward propagation approximation (Carrano et al., 2011) or the back propagation (BP) method (Sokolovskiy et al., 2002). The COSMIC team applied the BP method to geolocate the scintillation based on the GNSS high-rate (50–100 Hz) phase and amplitude data from the COSMIC-2 "scnPhs" product. Geolocation by BP is based on solving the wave equation in a vacuum by using the phase and amplitude, measured on the receiver trajectory as the boundary condition, and defining the direction of plasma irregularities using a magnetic field model. In the case of multiple bubbles along the transmitter-receiver line of sight, only the strongest bubble is detected by BP (e.g. Ludwig-Barbosa et al., 2023). In the current version of processing at the CDAAC, the BP technique is applied for each 10-s interval of COSMIC-2 high-rate scintillation data. The geolocation results (coordinates of the localized irregularities for those 10-s intervals with successful BP) are provided in the COSMIC-2 Level-2 "scnGeo" product. Wu et al. (2024) reported results of the validation analysis of the COSMIC-2 back-propagation geolocations by comparison to GOLD UV imaging data of equatorial plasma bubbles in the Atlantic/American longitudinal sector. It was found that the root mean square of the zonal difference between estimated geolocations of plasma irregularities with COSMIC-2 back propagation method and the locations of GOLD plasma bubbles was about 1.5° and for single intersection cases 0.5° in the magnetic longitude. It was also concluded that these geolocation data provide more accurate scintillation locations than the simpler method of assigning scintillations to the tangent point position.

We examined "scnGeo" files with successful BP geolocation results derived by the BP method applied to the COSMIC-2 high-rate phase and amplitude scintillation data. Figure 8 presents an overview of COSMIC-2 BP scintillation geolocations during 14–06 UT on 23–24 April 2023. Every red point represents the geographical position of the BP geolocation if it was successfully determined in 10-s intervals of high-rate data, so there is a significantly larger number of BP geolocation detections than amplitude S4max detections, which only include one value per occultation file (Sect. 4.4). Overall, a comparison of S4max and BP results (Fig. 7 vs. Fig. 8) shows a strong similarity, but BP geolocations provide much more detailed picture for areas affected by scintillations and better demonstrate the features of the storm-time EPBs evolution by tracing embedded small-scale irregularities, which are responsible for these amplitude scintillations. Figure 8 clearly illustrates that with the storm development from ~18 UT on 23 April 2023 until ~04 UT on 24 April 2023 an astonishing number of COSMIC-2 BP geolocations were detected in the African sector concentrated over the longitudinal range between 30°W and 30°E. The areas showing BP detections stretched significantly also in a

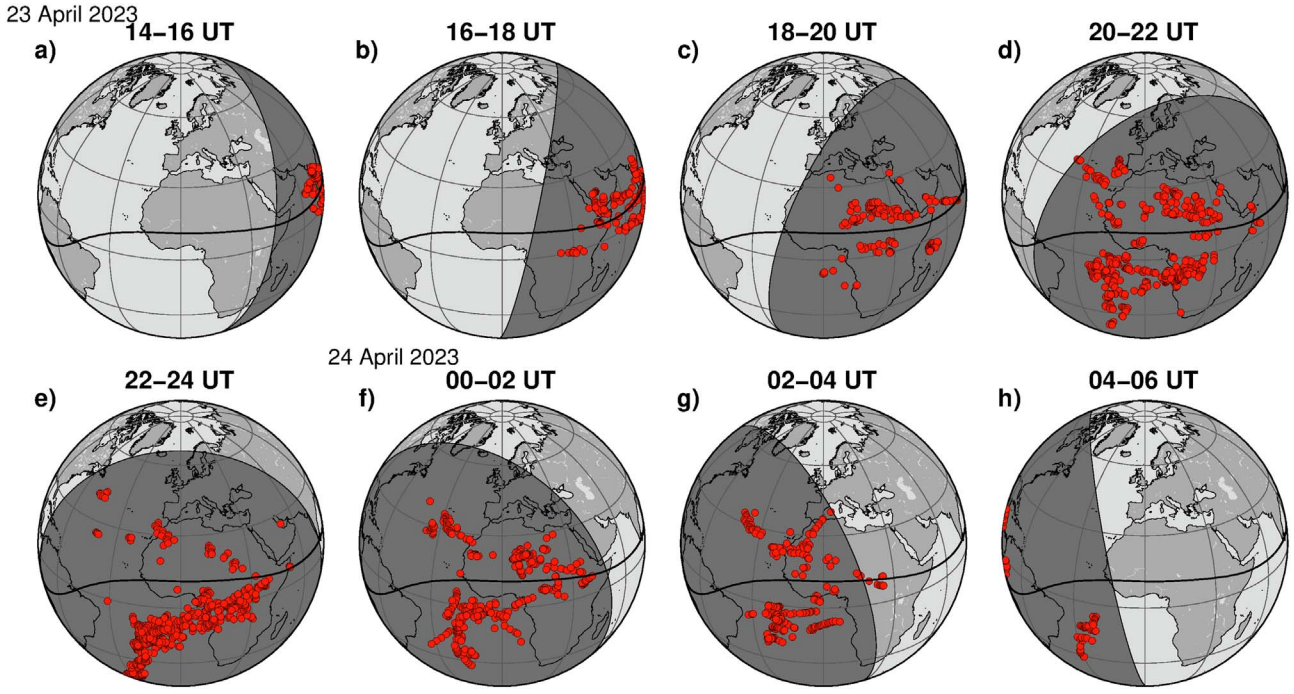

Figure 8. (a)–(h) COSMIC-2 back propagation geolocations as detected for specific 2-h time intervals during 14–06 UT on 23–24 April 2023. The central meridian is 0°, the grid has a 30° increment in latitude/longitude. The grey shading shows nighttime, the thick black line is the magnetic equator.

north-south direction, covering regions as far north as 30°–40°N including the Canary Islands (Spain), the Azores and Madeira Islands (Portugal), Northern Africa, and the Iberian Peninsula in southern Europe, and reaching as far south as 30°S in the southern Atlantic Ocean.

4.6 GOLD UV observations

Satellite UV imaging technology can also detect EPBs in the atomic oxygen 135.6-nm emission, which is proportional to ionospheric plasma density squared. The NASA GOLD imager is hosted onboard a geostationary satellite over the American sector (47.5°W longitude) and measures the Earth's UV airglow from ~120°W to ~20°E longitude (Eastes et al., 2019). We examined GOLD nighttime 135.6-nm emission images, available only between 20:10 UT and 00:30 UT each day, corresponding to ~19–22 LT over the scanned part of the Atlantic sector. Figure 9 shows a series of GOLD nighttime images captured between 20:10 UT and 22:55 UT on 23 April 2023. Bands of dark red/brown color at both sides from the equator mark the location of two crests of the EIA. EPB depletion signatures are associated with the appearance of dark, narrow stripes elongated between two peaks of the evening EIA. In the first scans available after 20:10 UT on 23 April 2023 (Figs. 9a–9c), there are signatures of several EPBs already formed near 0°–15°W over western Africa. EPB depletions, typically stretching between inner (equatorward) edges of two EIA crests, now deeply intrude into, and even surpass, the EIA crests. One of the most prominent plasma depletions developed near 15°W longitude; its southernmost part surpassed the southern EIA crest extending to ~30°S in GOLD scans during 20:10–21:10 UT (Figs. 9a–9e). Subsequent GOLD images, scanning regions further to the west, showed the continued evolution of plasma density depletions with a very pronounced westward tilt towards the central Atlantic Ocean in the Northern Hemisphere (Figs. 9e–9h). These depletion structures, largely expanded from the EIA zone to higher latitudes, were symmetric with respect to the magnetic equator, forming an inverted C-shape, typical for the storm-time EPBs. After 22 UT, GOLD scans showed an absence of newly formed intense EPBs in the central Atlantic beyond 20°–30°W longitude. This aligns well with COSMIC-2 detections showed that EPBs were confined to the 30°W–30°E longitude range. These scans continued to show significant plasma density depletion near 15°W longitude, extending as far poleward as 40°N and 35°S. The inverted C-shape of this giant depletion and its localization align well with the westward extension of the ionospheric irregularities observed in ground-based ROTI data (Figs. 2c–2f) and areas showing high concentration of COSMIC-2 detections of increased amplitude scintillations and BP geolocations over the Atlantic Ocean (Figs. 7d–7e, 8d–8e).

4.7 Vertical sounding station – El Arenosillo ionosonde in southern Spain

For many decades, the ionosonde observations have been utilized to detect equatorial Spread-F (ESF) associated with EPB occurrence over the ionosonde location at equatorial and low latitudes. We examined the indications of ionospheric irregularity presence in the data recorded by the southernmost ionosonde station in Europe, the El Arenosillo DPS-4D digisonde (digital ionosonde). Located in southern Spain, it has coordinates (37.1°N; 6.7°W; 27.6° MLAT). The position of this station was also shown by a blue asterisk in Figure 3a, when we

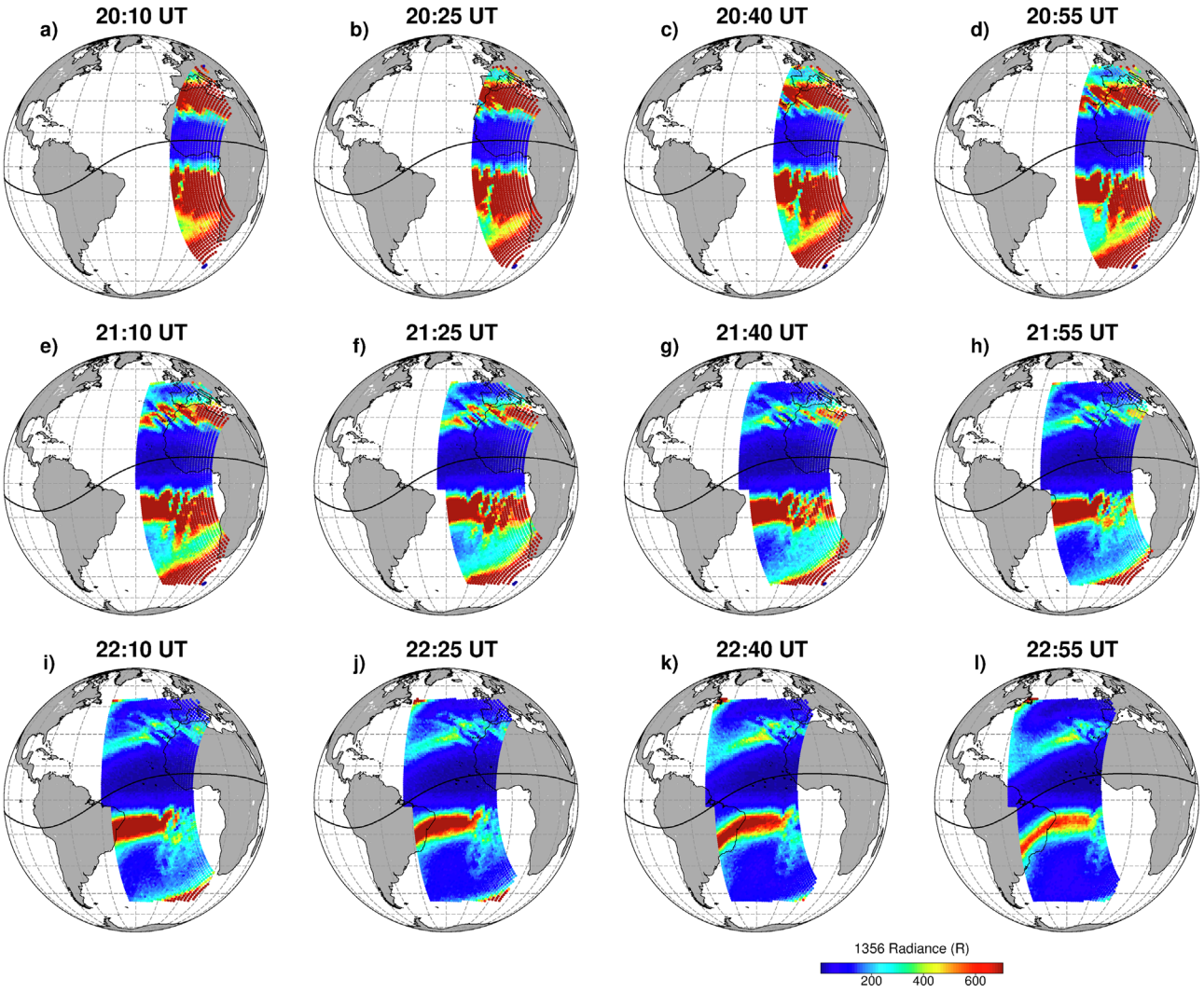

Figure 9. GOLD nighttime images of the 135.6-nm emission of atomic oxygen at various times between 21:10 UT and 22:55 UT on 23 April 2023. The central meridian is 30°W, the grid has 15° increment in latitude/longitude.

discussed GNSS ROTI observations over this region. The recorded ionograms are accessible through the DIDbase (Digital Ionogram DataBase; https://giro.uml.edu/didbase/) Web Portal from the GIRO (Global Ionospheric Radio Observatory; Reinisch & Galkin, 2011). The digisondes provide digital ionogram records, which show variations of the virtual height (h′) of the reflection from the ionospheric layers as a function of the radio frequency in MHz. From the digisonde observations, the true F2 peak height and true height vertical electron density profiles Ne(h) can be obtained from the true height inversion analysis using special software, e.g. ARTIST (Automated Real Time Ionogram Scaler with True height), or the expert ionogram interpretation tool SAO Explorer (Reinisch & Galkin, 2011).

Figure 10 illustrates so called "profilograms" derived from the ionosonde observations, which represent distribution of ionospheric density formulated in plasma frequency domain as a function of altitude (true height) and UT. The profilograms were constructed using the true-height vertical electron density profiles, which were selected at 10-min interval and manually scaled with the SAO Explorer tool. The data in Figure 10a corresponds to the reference quiet day of 22 April 2023. The normal diurnal changes in electron density's vertical distribution, typical for middle latitudes and that season, are clearly visible here. During night hours (21–24 UT and 00–05 UT; here UT is close to LT), the F2 layer rises to 400–450 km, then before sunrise it descends to 250–300 km, with peak density and layer thickness reaching its daily lows. After sunrise, the peak density and layer thickness gradually rise, reaching a maximum in the afternoon (13–16 UT) with the F2 layer peak located at ~300 km altitude.

The ionospheric behavior exhibited significant changes based on the profilogram for the storm day, 23 April 2023 (Fig. 10b). After 12 UT, the plasma density in the F2 layer increased and the layer uplifted with the F2 peak reaching 350–400 km. These effects can be explained by the positive phase of the ionospheric storm. Between 15 and 20 UT, the profilogram indicates fluctuations in the F2 layer peak altitude,

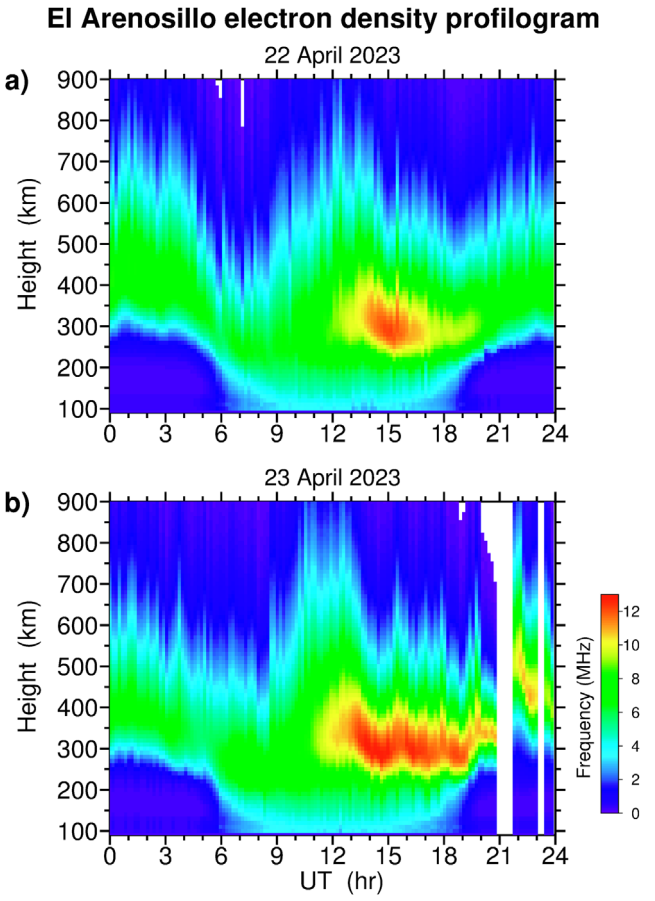

Figure 10. Profilograms of electron density as recorded by the El Arenosillo digisonde (37.1°N; 6.7°W; 27.6° magnetic latitude) in Spain, on (a) 22 April 2023 (pre-storm day) and (b) 23 April 2023 (storm day).

possibly due to the propagation of large-scale travelling ionospheric disturbances. Altadill et al. (2020) and Reinisch et al. (2018) provided an explanation of similar effects in the ionosonde profilograms. There is a gap between 20:45 and 21:45 UT, during which it was impossible to invert ionograms to electron density profiles due to Spread-F conditions. After 21:45 UT, the profilogram shows a huge jump in the F2 layer altitude, the layer lifted to the altitude of ~600 km with a rather high peak density (electron plasma frequency ~10 MHz), which is not typical for nighttime conditions over this ionosonde location at middle latitudes, even during a severe geomagnetic storm. Such uplift could be a sign of eastward-directed PPEFs appearing at midlatitudes. Until the end of the day, the F2 layer remained at high altitudes of 400–500 km with elevated F2 peak density (electron plasma frequency near 10–11 MHz).

Next, we analyzed the ionogram recordings to identify signatures of storm-induced ionospheric irregularities over southern Spain. Figure 11 presents series of the ionograms recorded by the El Arenosillo digisonde during 19:30–02:30 UT on 23–24 April 2023. The first plot corresponding to 19:30 UT shows a clear ionogram with well recognized ordinary (O-mode polarization) and extraordinary (X-mode) components of soundings reflections and the F2 layer critical frequency foF2 at 10.7 MHz. After 21:00 UT, the ionograms show diffuse reflections of the Mixed Spread-F type combining Frequency and Range Spread-F signatures with broad reflections in both frequency and range in both O-mode and X-mode traces. Such Spread-F conditions represent a rare phenomenon for the midlatitude ionosphere. Most frequently such effects can be seen during geomagnetic disturbances when the auroral irregularities zone expand from high to midlatitudes, or at equatorial stations during EPB events. The ground-based ROTI observations clearly demonstrated that auroral irregularities did not reach such low latitudes during the main phase of the storm (Figs. 2 and 3). So, these Spread-F conditions are likely linked to the occurrence of storm-induced post-sunset equatorial ionospheric irregularities. In the ionosonde area, irregularities were detected from ~21 UT on 23 April until ~02 UT on 24 April 2023. By 02:30 UT, the ionospheric conditions began transitioning back to a regular nighttime state with no Spread-F echoes and low foF2 values decreased to 4.0–4.5 MHz.

4.8 Scintillation receiver in southern Italy

While there are thousands of modern geodetic GNSS receivers operating in the world, the number of specialized scintillation receivers that operate permanently is quite small, only several dozen. The scintillation receivers are predominantly installed at equatorial and high latitudes, where the strongest scintillations occur. As a result, very few scintillation receivers are in regular operation at midlatitudes worldwide. Fortunately, one of these receivers is currently operational in southern Europe at Lampedusa, Italy, with coordinates (35.52°N, 12.63°E; 26.5° MLAT). The scintillation data is available at the electronic Space Weather upper atmosphere (*eSWua*, http://www.eswua.ingv.it/) data portal managed by INGV (Upper Atmosphere and Radio Propagation Working Group, 2020).

Figure 12 presents amplitude (S4) and phase (sigma_phi) scintillation data collected by the Septentrio PolaRx5S scintillation receiver at Lampedusa on 22–24 April 2023. The scintillation indices were computed using samples measured at 50 Hz rates for intervals of 60 s. Data was plotted for three GNSS systems – GPS, GLONASS, and Galileo. We used an elevation angle cut-off of 20°. Over these three days, there is a distinct period characterized by increased scintillation activity, showing intense amplitude (S4 > 0.5) and phase (sigma_phi > 0.5 rad) scintillations. The scintillation event lasted for several hours from ~19:30 UT until ~23:00 UT on 23 April 2023. The strong scintillations were detected on GNSS links with azimuths between 150° and 250°, which corresponded to south and south-westward directions. The scintillation receiver is located rather close to the El Arenosillo ionosonde in Spain, at a latitude nearly the same and approximately 6 degrees east, into the Mediterranean Sea. It is likely that the detected scintillations are linked to the ionospheric irregularities observed at that time over Spain and Northern Africa.

These results provide observational evidence that phase and amplitude scintillations were detected from the ground in southern Europe during the main phase of the storm.

4.9 EGNOS performance

It is important to emphasize that investigation of the events with equatorial plasma bubble occurrences at midlatitudes is not

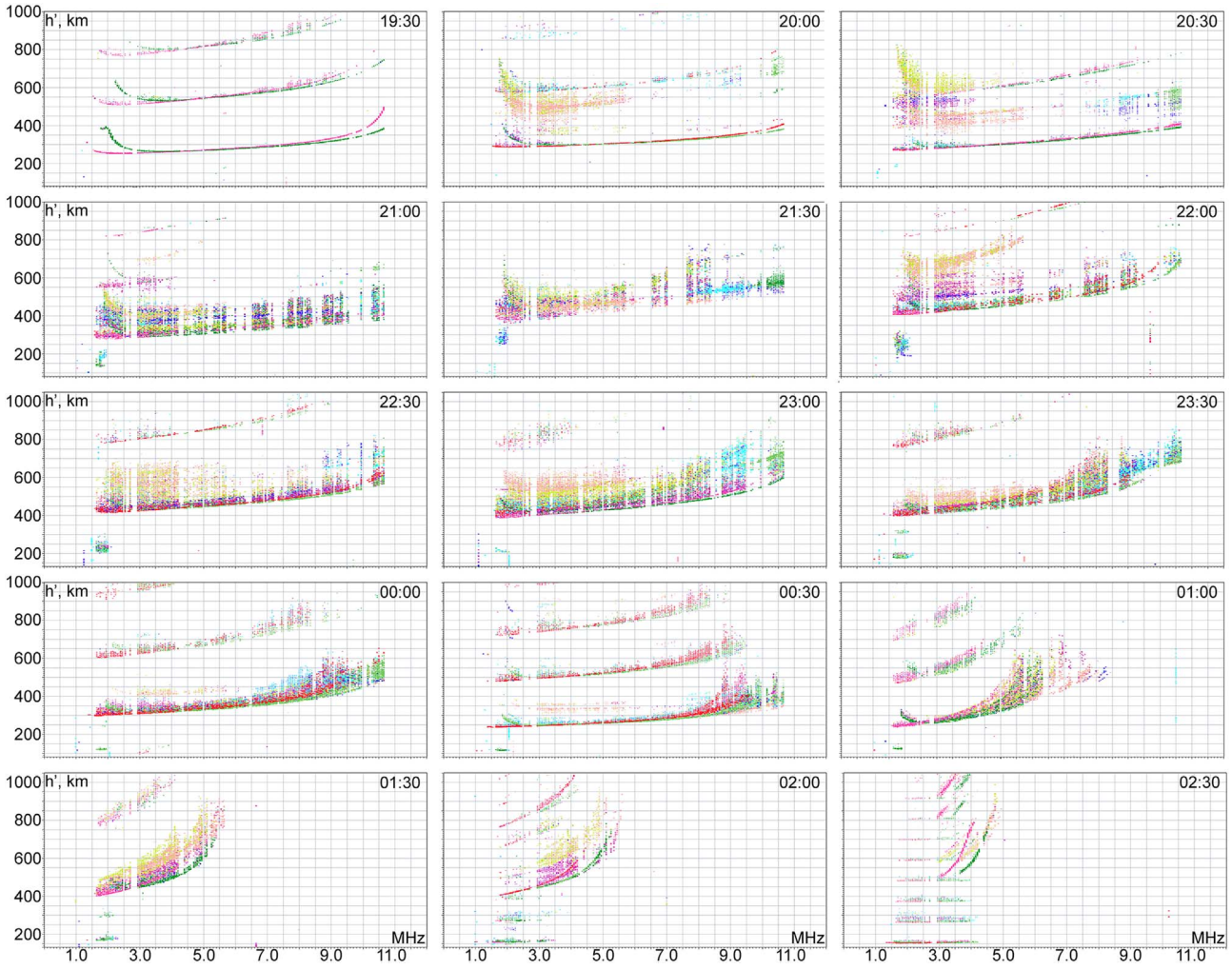

Figure 11. Sequence of vertical ionograms (virtual height in km vs. frequency in MHz) recorded by the El Arenosillo digisonde (37.1° N; 6.7° W; 27.6° magnetic latitude) in Spain, during 19:30–02:30 UT on 23–24 April 2023. The O-mode polarization is shown by red trace, the X-mode by green trace, and diffuse echoes correspond to spread-F conditions.

just a research interest. These bubbles have a direct impact on the performance of the ground-based systems that rely on transionospheric radio wave propagation, particularly on GNSS signals. For example, during the September 2017 geomagnetic storm, the storm-induced EPBs that occurred at North America midlatitudes, elongated across the continental US area and reached ~45°MLAT (Zakharenkova & Cherniak, 2020). Assessment of the impact of the storm-induced ionospheric irregularities on GPS-based kinematic positioning for 4500+ ground-based stations at equatorial and middle latitudes of the American sector revealed a large increase in 3-D kinematic positioning errors from the normal cm to dm level of accuracy to several meters for ground-based GPS stations that were near the storm-induced plasma density depletion (Zakharenkova & Cherniak, 2021). Amplitude and phase scintillations associated with passage of this plasma density depletion over the US midlatitudes were also reported in Mrak et al. (2020); Nishimura et al. (2021). During this storm, a decrease in positioning accuracy was also registered for several base stations of the Wide Area Augmentation System (WAAS; FAA GPS Performance Analysis Reports, Report #99, 2017). Maximum horizontal/vertical accuracies were 5/8 m for Miami and Atlanta – which is two to three times larger than the average error values over three months. For the June 2015 geomagnetic storm, Cherniak & Zakharenkova (2016) reported that occurrence of the unexpected super plasma bubbles at European midlatitude had affected GNSS availability for a number of users and led to performance degradation of the European Geostationary Navigation Overlay Service (EGNOS).

EGNOS is the European SBAS (Satellite Based Augmentation System) to GPS and GLONASS, and it is an analogue of FAA WAAS in the US EGNOS augments the GPS system and makes it suitable for safety-critical applications such as flying aircraft, navigating ships through narrow channels, railways, agriculture, etc. It allows users in Europe to determine their position with accuracy within 1.5 m. The initial configuration of the EGNOS ground-based segment includes 34 RIMS (Ranging Integrity Monitoring Stations) sites located over a wide geographical area. The main function of the RIMS is to collect measurements from GPS satellites and to transmit these

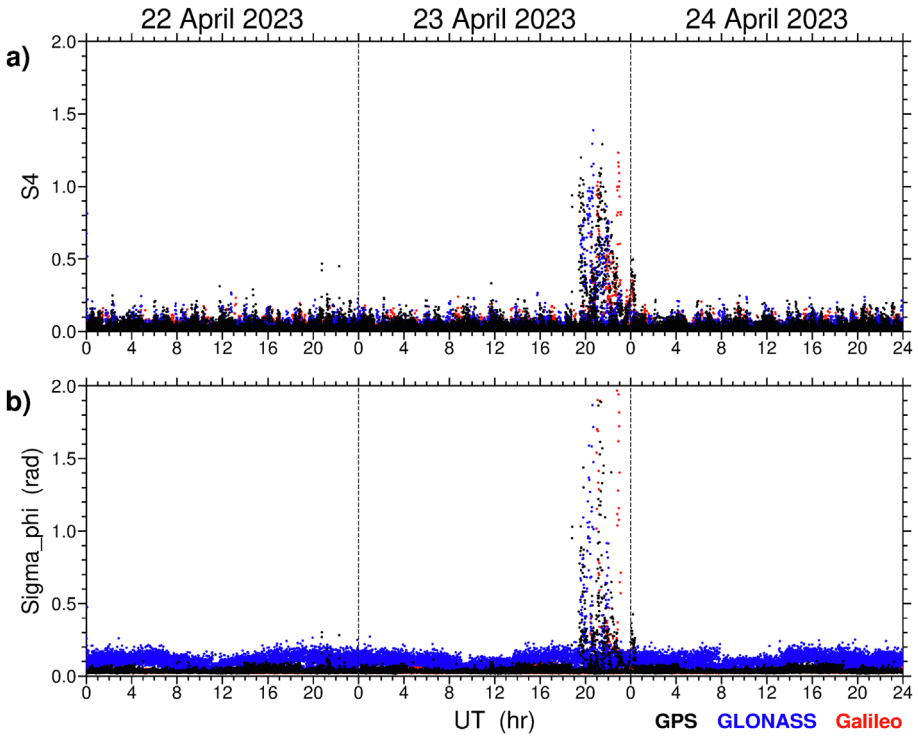

Figure 12. Time series of (a) amplitude (S4) and (b) phase (sigma_phi) scintillation measurements for every GNSS satellite in view with elevation above 20° as recorded by the Septentrio PolaRx5S scintillation receiver at Lampedusa (35.52°N, 12.63°E; 26.5° magnetic latitude) in southern Europe during 22–24 April 2023. Data plotted for three GNSS systems: GPS, GLONASS and Galileo (color-coded).

raw data every second to the Central Processing Facilities. Figure 13 presents daily summary plots with Horizontal and Vertical Navigation System Errors (HNSE and VNSE, respectively) for each RIMS sites, comparing status results for the pre-storm day of 22 April 2023 and the storm-day of 23 April 2023. The Navigation System Errors must be understood as the difference between the true position and the estimated position, and the presented figures include the percentile 95 of this NSE (represented by the color scale) and the standard deviation of the NSE distribution (represented by the size of the circles) at every RIMS.

Figures 13a–13b depict the usual quiet-day conditions, showing small positioning errors across all continental European RIMS sites. During the storm day (Figs. 13c–13d), there was a noticeable increase in vertical and horizontal errors registered at RIMS sites in higher northern latitudes, such as KIR (Kirkens, Norway), TRO (Tromsoe, Norway), RKK (Reykjavik, Iceland), JME (the island of Jan Mayen, Norway). The degradation effect observed here is consistent with what is typically expected during geomagnetic disturbances – direct impact of intense high-latitude irregularities occurrence linked to the expansion of the auroral oval zone that receives the main part of the magnetospheric particle precipitation. However, the largest errors in both horizontal and vertical planes were registered not in the northern high-latitude stations, but at the most southern RIMS sites of the EGNOS network. The increased errors (more than 2–3 m) were observed at RIMS sites located in Northern Africa at DJA (Djerba, Tunisia) and AGA (Agadir, Morocco), in the Iberian Peninsula at LSB (Lisbon, Portugal) and MLG (Malaga, Spain), and in the nearby islands at MAD (Madeira, Portugal), LPI (La Palma, Spain) and CNR (Canary Isl., Spain). All these locations matched exactly with areas affected by storm-induced ionospheric irregularities that were detected by ground-based GNSS and space-borne multi-instrument observations.

Previously, rather similar effect on EGNOS performance was reported for the case of super-bubbles occurrence during the June 2015 geomagnetic storm (Cherniak & Zakharenkova, 2016). Potentially, this suggests a repeatable pattern in how the super plasma bubbles reaching Europe impact on EGNOS positioning errors, which needs further investigation.

5 Discussion

In this paper, we investigated the ionospheric response to the 23–24 April 2023 geomagnetic storm. One of the significant features of this response was the development of the storm-induced super plasma bubbles, which extended extensively from equatorial to middle latitudes in the European/African sector during the early stage of the storm. Such extreme extension of latitudinal span indicates that those equatorial plasma bubbles also rise to greater altitudes above the equator (apex height of EPB). This rise is connected to the strength of the ionospheric vertical drift $\boldsymbol{E}\times\boldsymbol{B}$, which is primarily controlled by the eastward electric field. During geomagnetic storms, Prompt Penetrating Electric Fields (PPEFs) can instantly impact the equatorial ionosphere and the occurrence of regular post-sunset

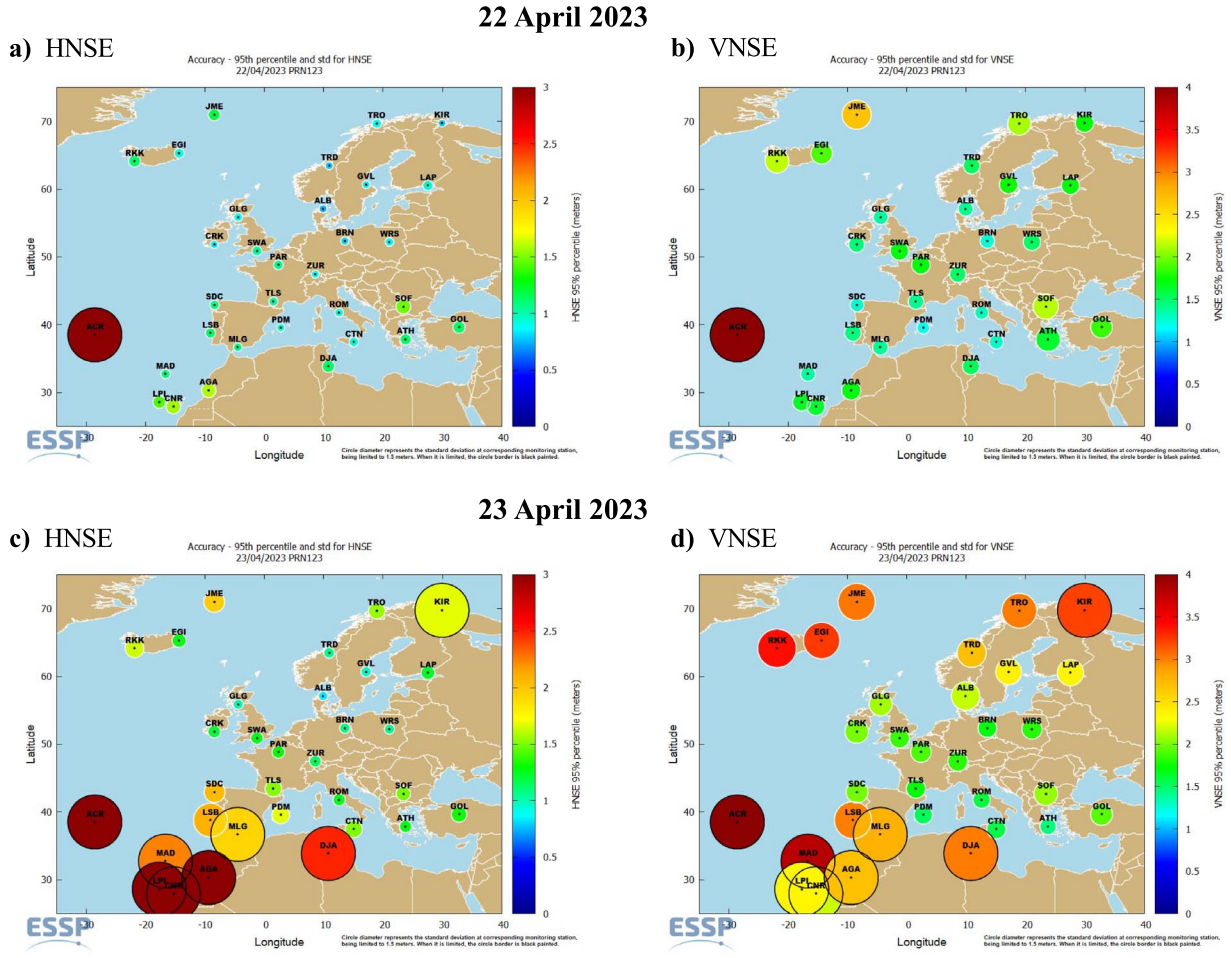

Figure 13. EGNOS performance summary plot with daily Horizontal and Vertical Navigation System Errors (HNSE and VNSE, respectively) for each station on (top) 22 April (pre-storm day) and (bottom) 23 April 2023 (storm day). Circle diameter indicates the standard deviation at corresponding monitoring station, being limited to 1.5 m; when it is limited, the circle border is black.

EPBs (e.g. Fejer et al., 1999; Huang, 2023). In the dusk sector, eastward PPEFs can amplify the regular pre-reversal enhancement, resulting in a more dramatic development of EPB due to much larger uplift of the ionosphere to higher altitudes where the Rayleigh–Taylor instability growth rate is maximized. PPEFs are generally associated to the sudden southward turn of the IMF Bz. PPEFs are transmitted from high latitudes to the equator near instantly and typically last a very short time (~30 min) because of the shielding effect in the ring current. However, effective shielding by the ring current may only occur once the IMF turns northward, and if the IMF remains steady southward, PPEFs can persist for hours (Huang et al., 2005, 2010). In our case, the IMF Bz was close to −5 nT just before the storm started at ~17:45 UT. Following that, IMF Bz quickly turned even more southward, reaching −20 nT, and remained steadily southward (from −20 to −25 nT) for several hours until ~21 UT on 23 April 2023 (Fig. 1). Hence, favorable conditions for PPEFs are observed from at least ~17:45 until ~21:00 UT on 23 April 2023. The COSMIC-2 in situ plasma density observations also demonstrated that intense plasma density depletions started to form in the African sector after 18 UT and their further expansion to westward longitudes (with progression of the sunset terminator) lasted until ~21 UT, finishing at ~30°W without further westward propagation afterwards over the Atlantic sector (Fig. 5).

Another important indicator for PPEF is the growth rate of the ring current under southward IMF Bz conditions. According to Basu et al. (2001), when there is a sudden intensification of the ring current, causing the SYM-H to decrease rapidly with the rate of change of order −50 nT/h, the PPEFs penetrating from high to lower latitudes cause the formation of ionospheric irregularities in the midlatitude and the equatorial region. Moreover, the dusk sector corresponding to the UT interval between the fast decrease of the SYM-H index and minimum SYM-H value determines uniquely the longitude range occupied by equatorial plasma bubbles and plasma density depletions.

During that phase of the April 2023 geomagnetic storm, when the IMF Bz turned southward, the SYM-H decreased from −49 nT at ~17:45 UT to −116 nT at ~19:00 UT on 23 April 2023 with the initial rate of change of −52 nT/h. The SYM-H reached an intermediate minimum of −121 nT at 19:27 UT and then dropped even further to a second minimum of −170 nT registered at 21:30 UT. During time interval between 17:45 UT and 19:30 UT, the longitude range of the

dusk/sunset (EPB generation sector) shifted from the starting area at ~15°–30°E to ~15°W–0°W, thus continuously covering the longitudinal span where signatures of the intense ionospheric irregularities were detected by the ground-based GNSS ROTI observations, Swarm and COSMIC-2 in situ density observations.

We should mention that for the case of super-bubbles detection in Europe during the June 2015 geomagnetic storm, the IMF Bz turned southward at 18:38 UT, dropping from 0 nT to −30 nT, and remained southward until ~20:00 UT, the SYM-H dropped from 88 nT at 18:37 UT to −139 nT at 20:17 UT on 22 June 2015 with the rate of change of −136 nT/h (Cherniak & Zakharenkova, 2016; Cherniak et al., 2019). Campuzano et al. (2023) reported observations of the storm-induced ionospheric irregularities over the Iberian Peninsula, Spain for two moderate geomagnetic storms in February 2014 and September 2021. According to the OMNIWeb database, for conditions of 17 September 2021, the IMF Bz turned southward at 17:57 UT to the level of −12 to −14 nT, and remained southward until ~21:20 UT, the SYM-H dropped from 10 nT at 18:25 UT to −65 nT at 20:46 UT and then −73 nT at 21:21 UT with the initial rate of change of −32 nT/h. For conditions of 27 February 2014, the IMF Bz turned southward at 18:20 UT from +13 nT to the level of −16 nT, and remained southward until ~22:56 UT, the SYM-H dropped from 3 nT at 18:14 UT to −46 nT at 19:42 and then −101 nT at 23:24 UT with the initial rate of change of −33 nT/h.

Thus we can conclude that favorable conditions for formation of storm-induced super-bubbles capable of extending to midlatitudes, specifically to the Iberian Peninsula in Europe, can occur when some necessary conditions are met: (1) the IMF Bz southward turn occurs between ~17 UT and 19 UT and IMF Bz remains southward for at least 1–2 h; (2) during the main phase of a storm, the rapid SYM-H decrease should also occur between 17 UT and 20 UT. The SYM-H decrease with the rate of change as low as −30 nT/h may be sufficient for that phenomenon development. If these conditions occur in later UT hours, the storm-induced EPBs may develop more westward, over the Atlantic Ocean, and hence will not affect the continental European sector.

The zonal coverage of the super-bubble occurrence is another important question, as it can vary considerably between geomagnetic storms. As mentioned above, the longitude range occupied by the storm-time EPBs is tied to LT, specifically the dusk sector location during the PPEF event. Earlier studies suggested that super plasma bubbles might occur only within a rather narrow range of ~15–20° in longitude related to the location of dusk sector during the PPEF, which was supposed to last short time (~30 min) because of the shielding effect in the ring current. Huang et al. (2005) reported that the interplanetary electric field could continuously penetrate to the low-latitude ionosphere without shielding for many hours, as long as the magnetic activity intensifies during storms. Therefore, potentially eastward-directed PPEFs may last for hours during the storm's main phase and favorable conditions for storm-time EPB generation might emerge at adjacent longitudes following the sunset terminator passage. Basu et al. (2007) suggested that the longitude interval populated by EPBs is determined by longitudes where the dusk sector occurs during the main phase of the storm, between the fast decrease of the SYM-H index and minimum SYM-H value. Cherniak et al. (2019) reported occurrence of two super bubble events during the June 2015 geomagnetic storm, one of small longitudinal coverage of ~20° in the European/African sector and second one of large longitudinal coverage of ~100° in American/Pacific sector. They discussed the relationship between the longitude range populated by EPBs and the duration of PPEFs – the first event occurred when southward IMF Bz lasted for a short time (~1 h), while the second event happened during a prolonged period of southward IMF Bz (~4 h). Discussing the super-EPBs occupying ~45° longitude range in the Asian sector during the December 2023 storm, Sun et al. (2024) also highlighted that the zonal coverage of super-EPBs during geomagnetic storms could be closely related to the duration of southward IMF Bz during the storm's main phase, and the occurring region of the EPB should be over the longitudes where local sunset coincides with southward IMF Bz. In the present study, the storm-time EPBs were found to occupy the longitudinal range of ~60° (~6,000 km), their development coincided with the prolonged period of the steady southward IMF Bz (−20 to 25 nT) during ~3 h between 18 and 21 UT on 23 April 2023 during growing main phase of the storm. The obtained results support the suggested relationships between duration of PPEF and southward IMF Bz during the main phase and an increase in the zonal coverage of the storm-time EPB occurrence.

The occurrence of storm-induced ionospheric irregularities associated with equatorial super bubbles extending towards midlatitudes is very difficult to predict since it depends on a poorly understood combination of factors including time of local sunset, time and intensity of penetrating electric fields, ambient plasma density, etc. It is important to emphasize the following: (1) storm-induced super plasma bubbles can occur even in the non-bubble seasons, and can differ from EPB climatology and EPB climatological models; (2) their effects can be more pronounced in the solar minimum conditions; (3) these structures can persist for many hours through the night and even after local sunset; (4) super plasma bubbles can occur at different longitudinal sectors during the same storm; (5) latitudinal dimensions and apex altitudes of super EPBs exceed significantly these parameters for the regular post-sunset EPBs.

We can also note that under such favorable conditions of eastward PPEFs occurring in the dusk sector and aiding in generation of very intense EPBs, the major features of super plasma bubbles – like rapid generation in the post-sunset period, extreme expansion towards midlatitudes of both hemispheres, persistence for a prolonged period, and slight westward drift – might be rather similar across different longitudinal sectors. One of the key constraints in tracing major spatio-temporal signatures of super bubbles is the existing coverage by ground-based observational facilities. Our ability to detect signatures of super bubbles in both hemispheres simultaneously is exclusive to the American sector, spanning across the continents of North and South America. In the European/African sector, there are large observational gaps over most of the African continent and the Atlantic Ocean. In the Asian sector, the equatorial and southern conjugate zones are primarily over the Pacific Ocean, resulting in sparse coverage by ground-based instruments. That is why for super bubbles events reported in the Asian sector, they are most often discussed only in the context of northern segment of super bubbles detected partially over Japan (e.g. Ma & Maruyama, 2006) or China (e.g. Aa et al., 2018; Li et al., 2018; Sun et al., 2024). The similar problem exists in

the European/African sector with very limited abilities to trace super bubble structures in its equatorial and southern segments. In the American sector, generation of typical post-sunset EPBs, as well as storm-enhanced EPBs, has much stronger intensity and occurrence probability compared to other regions worldwide (e.g. Burke et al., 2004; Xiong et al., 2010), due to reduced strength of the magnetic field and enhanced conductivity gradient resulting from the energetic particle precipitation in the South Atlantic Magnetic Anomaly region (Abdu et al., 2005, 2008). In the American sector, the effect of the offset between the geomagnetic and geographic poles is the largest one and the reduced value of the magnetic field near the South Atlantic Magnetic Anomaly leads to enhanced plasma uplift and F region destabilization in the presence of eastward PPEFs during geomagnetic storms (Foster & Erickson, 2013). That is why in the American sector, the storm-time ionospheric effects might be more intense and complex, like simultaneous occurrence of super plasma fountain effect, huge plasma bite outs near the equator, Storm Enhanced Density, equatorward move of the main ionospheric trough with enhanced Sub-Auroral Polarization Stream (SAPS) electric fields, and storm-enhanced EPBs. Recently, a new pattern of storm-induced ionospheric irregularities behavior at midlatitudes in the American sector was found – poleward extended plasma density depletion channels (Aa et al., 2019; Zakharenkova & Cherniak, 2020). Under disturbed conditions, they can appear at North America low latitudes as a part of extended post-sunset super bubbles, and further, they can stream across the magnetic field lines in the northwestward direction from low latitudes toward the main ionospheric trough forming elongated plasma depletion channels at the midlatitudes of North America. The physical mechanisms behind this phenomenon are still not well understood, but these events occurred in the presence of intense SAPS and westward plasma drifts. The plasma depletions associated with an evolution of super bubbles can reach very high latitudes, extending as far poleward as 45°–49° MLAT, sometimes close to the main ionospheric trough, which suggest that depleted plasma flux tubes had an apex height of 6000–8000 km above the magnetic equator (Aa et al., 2019; Huang et al., 2007; Zakharenkova & Cherniak, 2020). Comparing with such an extreme and rare behavior of storm-induced super plasma bubbles, which are themselves a rare phenomenon, we can conclude that super bubbles generated in the European/African sector during the April 2023 storm had poleward expansion up to 30°–35° MLAT only and were characterized by a more typical inverse C-shape form in a latitude–longitude domain without clearly detected signatures of poleward streaming towards the main ionospheric trough. However, gaps in the data over mid-latitudes in the Atlantic Ocean can hinder a complete picture (see Figs. 2c–2e for 20–22 UT on 23 April 2023), because DMSP F16 and F17 satellites (not shown here, available at https://www.ncei.noaa.gov/data/dmsp-space-weather-sensors/access/) registered westward horizontal plasma drifts up to ~1–2 km/s, a signature of the enhanced SAPS presence, at 55°–65°N over the Atlantic Ocean during 18–20 UT on 23 April 2023. This could potentially aid in a greater elongation of post-sunset super bubbles, particularly given their observed extension into the sunlit ionosphere over the Atlantic Ocean, also visible in the GOLD UV scans as the largely tilted northern portions of super EPBs over the central Atlantic.

6 Summary

To summarize, the main findings from our multi-instrument investigations on super plasma bubbles occurrence during the April 2023 geomagnetic storm are:

1. Ground-based GNSS ROTI maps registered an occurrence of very intense ionospheric irregularities that spread far away from the magnetic equator towards the south and north, covering areas of Northern Africa and south-western Europe in the Northern Hemisphere. The longitude range occupied by irregularities was between 30°W and 30°E. The estimated apex height of plasma bubbles reached ~2000–3000 km. The ionospheric irregularities persisted for 5–6 h. The areas with equatorial ionospheric irregularities in southern Europe show no connection to high latitude auroral irregularities.

2. The Swarm and COSMIC-2 satellites measured ionospheric in situ plasma density at ~500–550 km altitude, revealing the formation of intense ionospheric irregularities after the storm onset in the European/African sector spanning between 30°W and 30°E in longitude and extending as far poleward from the magnetic equator as ~30°–35° in both hemispheres. The large extension of these ionospheric structures from equatorial to higher latitudes covered the range of EPB apex height from of ~1500 km to ~3000 km. Satellite data revealed extensive details about how storm-induced ionospheric irregularities evolved over the equatorial region, especially in areas with scarce ground-based observations (central Africa, ocean areas).

3. The amplitude S4 scintillation observations from the TGRS instrument onboard COSMIC-2 confirmed the presence of small-scale ionospheric irregularities, which produced amplitude scintillations on GNSS signals. After 20 UT on 23 April 2023, the amplitude scintillations with S4 exceeding 0.5–1.0 were detected over equatorial and low latitudes in the African/Atlantic sector, covering a broad longitude range between 30° and 30°E. Multiple detections with high S4 were registered in both hemispheres over a large area between ~35°N and ~30°S and persisted for several hours until at least 02 UT on 24 April 2023.

4. Another large dataset of scintillation detections, based on application the back propagation approach to the COSMIC-2 TGRS high-rate scintillation measurements, provides an even more detailed picture of areas affected by scintillations and of features of the storm-time EPBs evolution. The African longitudinal sector had a significant concentration of COSMIC-2 BP geolocations, mainly within the range of 30°W – 30°E. The areas where BP detections were found stretched extensively also in the north–south direction, covering regions as far north as 30°–40°N including the Canary Islands (Spain), the Azores and Madeira Islands (Portugal), Northern Africa, and the Iberian Peninsula in southern Europe, and reaching as far south as 30°S in the southern Atlantic Ocean. These areas with high density of BP geolocations showed a strong overlap with the locations of enormous plasma depletions seen in GOLD UV images.

5. Ionosonde data, from Spain's southernmost station El Arenosillo, showed strong F2 layer uplift and increased plasma density near its peak during the main phase of the storm. Between ~20 UT on 23 April and ~02 UT on 24 April 2023, the ionograms detected the Spread–F echoes, associated with the presence of storm-induced ionospheric irregularities in the ionosonde vicinity.

6. The scintillation receiver located in Lampedusa, Italy (southern Europe) registered strong amplitude and phase scintillations, coming from south and south-west directions, during 19:30–23:00 UT on 23 April 2023. Ionospheric irregularities seen over Spain and Northern Africa matched those directions precisely.

7. During this storm on 23 April 2023, the EGNOS performance degradation was found to be significantly greater (more than 2–3 m) in the southern area, which was affected by super plasma bubbles, while large errors are typically expected at northern stations of much higher latitudes due to occurrence of intense auroral irregularities with the storm development.

8. The longitudinal sector affected by the storm-induced EPBs directly depends on the UT time interval during which both the southward turn of IMF Bz and rapid decrease of the SYM-H index should happen. For the potential development of storm-induced EPBs in the European/African sector and chances to detect these signatures in the European region (if these irregularities extended far enough from the equator) – both these conditions should take place between 17 and 20 UT. The longer these conditions persist, the greater the chances that new EPBs will form further westward, trailing the sunset terminator and occupying a progressively larger longitudinal range.

The occurrence of the storm-induced ionospheric irregularities, which can extend from equatorial to middle latitudes under specific Space Weather conditions, is a phenomenon that is still unpredictable and not well understood, that demands further observational and simulation studies. This is the first study demonstrating great capabilities of the COSMIC-2 mission to assist in the integrated multi-instrument research of the storm-time super plasma bubble phenomenon.

Acknowledgements

We acknowledge COSMIC CDAAC for providing COSMIC-2 observations (https://www.cosmic.ucar.edu/what-we-do/cosmic-2/data; https://doi.org/10.5065/T353-C093). GNSS data are available with SONEL (ftp://ftp.sonel.org/gps/data), CORS (https://geodesy.noaa.gov/corsdata), EUREF (ftp://gnss.bev.gv.at/pub/obs/), Natural Resources Canada (webapp.geod.nrcan.gc.ca), SOPAC (ftp://garner.ucsd.edu), RBMC Brazil (https://geoftp.ibge.gov.br/informacoes_sobre_posicionamento_geodesico/rbmc/), SWEPOS (swepos.lantmateriet.se), IGN France (ftp://rgpdata.ign.fr), IGN Espana (https://datos-geodesia.ign.es), ReNEP Portugal (ftp://ftp.dgterritorio.pt/), Italian Geodetic Data Archiving Facility (ftp://geodaf.mt.asi.it), TrigNET (ftp://ftp.trignet.co.za). GOLD UV data are available at GOLD Science Data Center (https://gold.cs.ucf.edu/data/). Raw ionograms from DIDBase digisonde network are available through GIRO (http://giro.uml.edu/; http://spase.info/SMWG/Observatory/GIRO; Reinisch and Galkin, 2011) and were processed using the SAO Explorer tool (https://ulcar.uml.edu/SAO-X/SAO-X.html). Swarm observations are available through the ESA earth observation portal (ftp://www.swarm-diss.eo.esa.int/). The scintillation data from Lampedusa are available at the INGV electronic Space Weather upper atmosphere data portal (*eSWua*, http://www.eswua.ingv.it/). The historical EGNOS status information is available through EGNOS GSC-Europa portal (https://egnos.gsc-europa.eu/services/egnos-performance-viewer). The geophysical parameters data are available through NASA/GSFC Space Physics Data Facility's OMNIWeb service (https://omniweb.gsfc.nasa.gov/ow.html), GFZ-Potsdam (https://kp.gfz-potsdam.de/en/; Matzka et al., 2021) and SuperMAG (https://supermag.jhuapl.edu/; Gjerloev 2012). The authors acknowledge Dr. Lucilla Alfonsi and Dr. Luca Spogli for their valuable discussion on INGV Space Weather Service database. This study was supported by the National Science Foundation (Grant 2054356), National Aeronautics and Space Administration (Grant C22K0658), Air Force Contract FA8803-19-C-0004, and National Oceanic and Atmospheric Administration (Cooperative Agreement R4310383). The editor thanks two anonymous reviewers for their assistance in evaluating this paper.

References

Aarons, J, Mendillo M, Yantosca R, Kudeki E. 1996. GPS phase fluctuations in the equatorial region during the MISETA 1994 campaign. *J Geophys Res Space Phys* **101 (A12)**: 26851–26862. https://doi.org/10.1029/96ja00981.

Aarons, J, Mendillo M, Yantosca R. 1997. GPS phase fluctuations in the equatorial region during sunspot minimum. *Radio Sci* **32 (4)**: 1535–1550. https://doi.org/10.1029/97RS00664.

Aa, E, Huang W, Liu S, Ridley A, Zou S, et al. 2018. Midlatitude plasma bubbles over China and adjacent areas during a magnetic storm on 8 September 2017. *Space Weather* **16 (3)**: 321–331. https://doi.org/10.1002/2017SW001776.

Aa, E, Zou S, Ridley A, Zhang SR, Coster AJ, Erickson PJ, Liu S, Ren J 2019. Merging of storm time midlatitude traveling ionospheric disturbances and equatorial plasma bubbles, *Space Weather* **17 (2)**: 285–298. https://doi.org/10.1029/2018SW002101.

Abdu, MA, Batista IS, Walker GO, Sobral JHA, Trivedi NB, de Paula ER. 1995. Equatorial ionospheric electric field during magnetospheric disturbances: Local time/longitude dependences from recent EITS campaigns. *J Atmos Terr Phys* **57**: 1065–1083. https://doi.org/10.1016/0021-9169(94)00123-6.

Abdu, MA, Batista IS, Takahashi H, MacDougall J, Sobral JH, Medeiros AF, Trivedi NB 2003. Magnetospheric disturbance induced equatorial plasma bubble development and dynamics: A case study in Brazilian sector. *J Geophys Res Space Phys* **108 (A12)**: 1449. https://doi.org/10.1029/2002JA009721.

Abdu, MA, Batista IS, Carrasco AJ, Brum CGM. 2005. South Atlantic magnetic anomaly ionization: A review and a new focus on electrodynamic effects in the equatorial ionosphere. *J Atmos Solar-Terrestrial Phys* **67**: 1643–1657. https://doi.org/10.1016/j.jastp.2005.01.014.

Abdu, MA, De Paula ER, Batista IS, Reinisch BW, Matsuoka MT, et al. 2008. Abnormal evening vertical plasma drift and effects on ESF and EIA over Brazil-South Atlantic sector during the 30 October 2003 superstorm, *J Geophys Res Space Phys* l**113 (7)**: A07313. https://doi.org/10.1029/2007JA012844.

Altadill, D, Segarra A, Blanch E, Juan JM, Paznukhov VV, Buresova D, Galkin G, Reinisch BW, Belehaki A. 2020. A method for real-time identification and tracking of traveling ionospheric disturbances using ionosonde data: First results. *J Space Weather Space Clim* **10**: 2. https://doi.org/10.1051/swsc/2019042.

Basu, S, Basu S, Mackenzie E, Whitney HE. 1985. Morphology of phase and intensity scintillations in the auroral oval and polar cap. *Radio Sci* **20 (3)**: 347–356. https://doi.org/10.1029/RS020i003p00347.

Basu, S, Basu S, Valladares CE, Yeh HC, Su SY, et al. 2001. Ionospheric effects of major magnetic storms during the International Space Weather Period of September and October 1999: GPS observations, VHF/UHF scintillations, and in situ density structures at middle and equatorial latitudes. *J Geophys Res Space Phys* **106 (A12)**: 30389–30413. https://doi.org/10.1029/2001ja001116.

Basu, S, Basu S, Groves KM, MacKenzie E, Keskinen MJ, Rich FJ. 2005. Near-simultaneous plasma structuring in the midlatitude and equatorial ionosphere during magnetic superstorms. *Geophys Res Lett* **32 (12)**. https://doi.org/10.1029/2004GL021678.

Basu S, Basu Su, Rich FJ, Groves KM, MacKenzie E, Coker C, Sahai Y, Fagundes PR, Becker-Guedes F. 2007. Response of the

equatorial ionosphere at dusk to penetration electric fields during intense magnetic storms. *J Geophys Res Space Phys* **112(8)**: A08308. https://doi.org/10.1029/2006JA012192.

Burke, WJ, Gentile LC, Huang CY, Valladares CE, Su SY. 2004. Longitudinal variability of equatorial plasma bubbles observed by DMSP and ROCSAT-1. *J Geophys Res Space Phys* **109**: A12301. https://doi.org/10.1029/2004JA010583.

Campuzano, SA, Delgado-Gómez F, Migoya-Orué Y, Rodríguez-Caderot G, Herraiz-Sarachaga M, Radicella SM. 2023. Study of ionosphere irregularities over the Iberian Peninsula during two moderate geomagnetic storms using GNSS and ionosonde observations. *Atmosphere* **14 (2)**: 233. https://doi.org/10.3390/atmos14020233.

Carrano, CS, Groves KM, Caton RG, Rino CL, Straus PR. 2011. Multiple phase screen modeling of ionospheric scintillation along radio occultation raypaths. *Radio Sci.* **46 (3)**: RS0D07. https://doi.org/10.1029/2010RS004591.

Cherniak, I, Krankowski A, Zakharenkova I. 2014. Observation of the ionospheric irregularities over the Northern Hemisphere: Methodology and service. *Radio Sci.* **49 (8)**: 653–662. https://doi.org/10.1002/2014RS005433.

Cherniak, I, Zakharenkova I. 2016. First observations of super plasma bubbles in Europe. *Geophys Res Lett.* **43 (21)**: 11137–11145. https://doi.org/10.1002/2016GL071421.

Cherniak, I, Krankowski A, Zakharenkova I. 2018. ROTI Maps: a new IGS ionospheric product characterizing the ionospheric irregularities occurrence. *GPS Solut* **22**: 69. https://doi.org/10.1007/s10291-018-0730-1.

Cherniak, I, Zakharenkova I, Sokolovsky S. 2019. Multi-instrumental observation of storm-induced ionospheric plasma bubbles at equatorial and middle latitudes. *J Geophys Res Space Phys* **124 (3)**: 1491–1508. https://doi.org/10.1029/2018JA026309.

Cherniak, I, Zakharenkova I. 2022. Development of the storm-induced ionospheric irregularities at equatorial and middle latitudes during the 25–26 August 2018 geomagnetic storm. *Space Weather* **20 (2)**: e2021SW002891. https://doi.org/10.1029/2021SW002891.

Dymond, KF. 2012. Global observations of L band scintillation at solar minimum made by COSMIC. *Radio Sci.* **47 (3)**: RS0L18. https://doi.org/10.1029/2011RS004931.

Eastes, RW, Solomon SC, Daniell RE, Anderson DN, Burns AG, England SL, Martinis CR, McClintock WE. 2019. Global-scale observations of the equatorial ionization anomaly. *Geophys Res Lett* **46 (16)**: 9318–9326. https://doi.org/10.1029/2019GL084199.

FAA GPS Performance Analysis Reports. 2017. *Report #99, Table 6-1*. https://www.nstb.tc.faa.gov/reports/PAN99_1017.pdf. Accessed 20 June 2024.

Fejer, BG, Scherliess L, de Paula ER. 1999. Effects of the vertical plasma drift velocity on the generation and evolution of equatorial spread F. *J Geophys Res Space Phys* **104 (A9)**: 19859–19869. https://doi.org/10.1029/1999ja900271.

Foster, JC, Erickson PJ. 2013. Ionospheric superstorms: Polarization terminator effects in the Atlantic sector. *J Atmos Solar-Terrestrial Phys* **103**: 147–156. https://doi.org/10.1016/j.jastp.2013.04.001.

Fremouw, EJ, Leadabrand RL, Livingston RC, Cousins MD, Rino CL, Fair BC, Long RA. 1978. Early results from the DNA Wideband satellite experiment – Complex-signal scintillation, *Radio Sci* **13 (1)**: 167–187. https://doi.org/10.1029/RS013i001p00167.

Gjerloev JW. 2012. The SuperMAG data processing technique. *J Geophys Res* **117**: A09213. https://doi.org/10.1029/2012JA017683.

Haerendel, G. 1974. *Theory of equatorial spread F. preprint*. Max-Planck Inst. für Extraterr. Phys., Munich, Germany.

Heelis, RA, Stoneback RA, Perdue MD, Depew MD, Morgan WA, Mankey MW, et al. 2017. Ion velocity measurements for the ionospheric connections explorer. *Space Sci Rev* **212 (1–2)**: 615–629. https://doi.org/10.1007/s11214-017-0383-3.

Huang, CS, Foster JC, Kelley MC. 2005. Long-duration penetration of the interplanetary electric field to the low-latitude ionosphere during the main phase of magnetic storms. *J Geophys Res Space Phys* **110**: A11309. https://doi.org/10.1029/2005JA011202.

Huang, CS, Foster JC, Sahai Y. 2007. Significant depletions of the ionospheric plasma density at middle latitudes: A possible signature of equatorial spread F bubbles near the plasmapause, *J Geophys Res Space Phys* **112 (5)**: A05315. https://doi.org/10.1029/2007JA012307.

Huang, CS, Rich FJ, Burke WJ. 2010. Storm time electric fields in the equatorial ionosphere observed near the dusk meridian. *J Geophys Res Space Phys* **115**: A08313. https://doi.org/10.1029/2009JA015150.

Huang, CS, La Beaujardiere OD , Roddy PA, Roddy PA, Hunton DE, Pfaff RF, Valladares CE, Ballenthin JO 2011. Evolution of equatorial ionospheric plasma bubbles and formation of broad plasma depletions measured by the C/NOFS satellite during deep solar minimum. *J Geophys Res* **116**: A03309. https://doi.org/10.1029/2010JA015982.

Huang, CS, De La Beaujardiere O, Roddy PA, Hunton DE, Ballenthin JO, Hairston MR. 2013. Long-lasting daytime equatorial plasma bubbles observed by the C/NOFS satellite. *J Geophys Res Space Phys* **118 (5)**: 2398–2408. https://doi.org/10.1002/jgra.50252.

Huang, CS. 2023. Identification of penetration and disturbance dynamo electric fields and their effects on the generation of equatorial plasma bubbles, *J Geophys Res Space Phys* **128**: e2023JA031766. https://doi.org/10.1029/2023JA031766.

Hysell DL. 2000. An overview and synthesis of plasma irregularities in equatorial spread F. *J Atmos Solar-Terrestrial Phys* **62 (12)**: 1037–1056. https://doi.org/10.1016/s1364-6826(00)00095-x.

Katamzi-Joseph, ZT, Habarulema JB, Hernández-Pajares M. 2017. Midlatitude postsunset plasma bubbles observed over Europe during intense storms in April 2000 and 2001. *Space Weather* **15 (9)**: 1177–1190. https://doi.org/10.1002/2017SW001674.

Kelley, M. 1989. *The Earth's ionosphere*. Academic Press: San Diego, p. 487,

Kintner, PM, Ledvina BM, De Paula ER, Kantor IJ. 2004. Size, shape, orientation, speed, and duration of GPS equatorial anomaly scintillations. *Radio Sci* **39 (2)**: RS2012. https://doi.org/10.1029/2003rs002878.

Ko, CP, Yeh HC. 2010. COSMIC/FORMOSAT-3 observations of equatorial F region irregularities in the SAA longitude sector. *J Geophys Res Space Phys* **115 (11)**: A11309. https://doi.org/10.1029/2010JA015618.

Li, G, Ning B, Zhao B, Liu L, Wan W, Ding F, Xu JS, Liu JY, Yumoto K. 2009. Characterizing the 10 November 2004 storm-time middle-latitude plasma bubble event in Southeast Asia using multi-instrument observations. *J Geophys Res Space Phys* **114 (7)**: A07304. https://doi.org/10.1029/2009JA014057.

Li, G, Ning B, Wang C, Abdu MA, Otsuka Y, Yamamoto M, Wu J, Chen J. 2018. Storm-enhanced development of postsunset equatorial plasma bubbles around the meridian 120 E/60 W on 7–8 September 2017, *J Geophys Res Space Phys* **123 (9)**: 7985–7998. https://doi.org/10.1029/2018JA025871.

Ludwig-Barbosa, V, Rasch J, Sievert T, Carlstroem A, Pettersson MI, Vu VT, Christensen J. 2023. Detection and localization of F-layer ionospheric irregularities with the back-propagation method

along the radio occultation ray path. *Atmos Meas Tech* **16**: 1849–1864. https://doi.org/10.5194/amt-16-1849-2023.

Ma, G, Maruyama T . 2006. A super bubble detected by dense GPS network at east Asian longitudes. *Geophys Res Lett* **33** (**21**): L21103. https://doi.org/10.1029/2006GL027512.

Martinis, C, Baumgardner J, Mendillo M, Wroten J, Coster A, Paxton L. 2015. The night when the auroral and equatorial ionospheres converged. *J Geophys Res Space Phys* **120**: 8085–8095. https://doi.org/10.1002/2015JA021555.

Matzka, J, Bronkalla O, Tornow K, Elger K, Stolle C. 2021. *Geomagnetic Kp index. V. 1.0. GFZ Data Services*. https://doi.org/10.5880/Kp.0001.

Mrak, S, Semeter J, Nishimura Y, Rodrigues FS, Coster AJ, Groves K. 2020. Leveraging geodetic GPS receivers for ionospheric scintillation science. *Radio Sci* **55** (**11**): e2020RS007131. https://doi.org/10.1029/2020RS007131.

Mukherjee, GK, Carlo L, Mahajan SH, Patil PT. 1998. First results of all-sky imaging from India. *Earth Planet Space* **50** (**2**): 119–127. https://doi.org/10.1186/BF03352093.

Nishimura, Y, Mrak S, Semeter JL, Coster AJ, Jayachandran PT, Groves KM, Knudsen DJ, Nishitani N, Ruohoniemi JM. 2021. Evolution of mid-latitude density irregularities and scintillation in North America during the 7–8 September 2017 storm. *J Geophys Res Space Phys* **126**: e2021JA029192. https://doi.org/10.1029/2021ja029192.

Pi, X, Mannucci AJ, Lindqwister UJ, Ho CM. 1997. Monitoring of global ionospheric irregularities using the worldwide GPS network. *Geophys Res Lett* **24** (**18**): 2283–2286. https://doi.org/10.1029/97GL02273.

Reinisch, BW, Galkin IA. 2011. Global ionospheric radio observatory (GIRO). *Earth Planet Space* **63** (**4**): 377–381. https://doi.org/10.5047/eps.2011.03.001.

Reinisch, B, Galkin I, Belehaki A, Paznukhov V, Huang X, Paznukhov V, Huang X, et al. 2018. Pilot ionosonde network for identification of traveling ionospheric disturbances. *Radio Sci* **53** (**3**): 365–378. https://doi.org/10.1002/2017RS006263.

Rodrigues, FS, Socola JG, Moraes AO, Martinis C, Hickey DA. 2021. On the properties of and ionospheric conditions associated with a mid-latitude scintillation event observed over southern United States. *Space Weather* **19** (**6**): e2021SW002744. https://doi.org/10.1029/2021SW002744.

Sokolovskiy, S, Schreiner W, Rocken C, Hunt D. 2002. Detection of high-altitude ionospheric irregularities with GPS/MET. *Geophys Res Lett* **29** (**3**): https://doi.org/10.1029/2001GL013398.

Sun, W, Li G, Lei J, Zhao B, Hu L, et al.. 2023. Ionospheric super bubbles near sunset and sunrise during the 26–28 February 2023 geomagnetic storm. *J Geophys Res Space Phys* **128** (**11**): e2023JA031864. https://doi.org/10.1029/2023JA031864.

Sun, W, Li G, Zhang SR, Hu L, Dai G, Zhao B, Otsuka Y, et al. 2024. Regional ionospheric super bubble induced by significant upward plasma drift during the 1 December 2023 geomagnetic storm. *J Geophys Res Space Phys* **129** (**6**): e2024JA032430. https://doi.org/10.1029/2024JA032430.

Tsunoda, RT, Livingston RC, McClure JP, Hanson WB. 1982. Equatorial plasma bubbles: Vertically elongated wedges from the bottomside F layer. *J Geophys Res* **87**: 9171. https://doi.org/10.1029/ja087ia11p09171.

Upper Atmosphere Physics and Radiopropagation Working Group, Cesaroni C, De Franceschi G, Marcocci C, Pica E, Romano V, Spogli L. 2020. *Electronic Space Weather upper atmosphere (eSWua) Database – GNSS scintillation data, Version 1.0, August 1, 2020*. Istituto Nazionale di Geofisica e Vulcanologia (INGV). Available at https://doi.org/10.13127/ESWUA/GNSS.

Weiss, JP, Schreiner WS, Braun JJ, Xia-Serafino W, Huang CY. 2022. COSMIC-2 mission summary at three years in orbit. *Atmosphere* **13**: 1409. https://doi.org/10.3390/atmos13091409.

Woodman, R, La Hoz C. 1976. Radar observations of F region equatorial irregularities. *J Geophys Res.* **81** (**31**): 5447–5466. https://doi.org/10.1029/JA081i031p05447.

Wu, Q, Pedatella NM, Braun JJ, Schreiner W, Weiss J, Chou MY, et al. 2022. Comparisons of ion density from IVM with the GNSS differential TEC-derived electron density on the FORMOSAT-7/COSMIC-2 mission. *J Geophys Res Space Phys* **127** (**8**): e2022JA030392. https://doi.org/10.1029/2022JA030392.

Wu, Q, Braun J, Sokolovskiy S, Schreiner W, Pedatella N, Weiss JP, Cherniak I, Zakharenkova I 2024. GOLD plasma bubble observations comparison with geolocation of plasma irregularities by back propagation of the high-rate FORMOSA7/COSMIC 2 scintillation data. *Front Astron Space Sci* **11**: 1407457. https://doi.org/10.3389/fspas.2024.1407457.

Xiong, C, Park J, Lühr H, Stolle C, Ma SY. 2010. Comparing plasma bubble occurrence rates at CHAMP and GRACE altitudes during high and low solar activity. *Ann Geophys* **28** (**9**): 1647–1658. https://doi.org/10.5194/angeo-28-1647-2010.

Zakharenkova I, Astafyeva E, Cherniak I. 2016. GPS and GLONASS observations of large-scale traveling ionospheric disturbances during the 2015 St. Patrick's Day storm. *J Geophys Res Space Phys* **121** (**12**): 12138–12156. https://doi.org/10.1002/2016JA023332.

Zakharenkova, I, Cherniak I. 2020. When plasma streams tie up equatorial plasma irregularities with auroral ones. *Space Weather* **18** (**2**): e2019SW002375. https://doi.org/10.1029/2019SW002375.

Zakharenkova, I, Cherniak I. 2021. Effects of storm-induced equatorial plasma bubbles on GPS-based kinematic positioning at equatorial and middle latitudes during the September 7–8, 2017, geomagnetic storm. *GPS Solut.* **25** (**4**): https://doi.org/10.1007/s10291-021-01166-3.

Zakharenkova, I, Cherniak I, Braun JJ, Wu Q. 2023. Global maps of equatorial plasma bubbles depletions based on FORMOSAT-7/COSMIC-2 ion velocity meter plasma density observations. *Space Weather* **21** (**5**): e2023SW003438. https://doi.org/10.1029/2023SW003438.

Cite this article as: Zakharenkova I, Cherniak I, Braun JJ, Wu Q, Sokolovskiy S, et al. 2025. Multi-instrument observations of ionospheric super plasma bubbles in the European longitude sector during the 23–24 April 2023 severe geomagnetic storm. *J. Space Weather Space Clim.* **15**, 5. https://doi.org/10.1051/swsc/2025001.